Nano-FET-enabled biosensors: Materials perspective and recent advances in North America

Mohammed Sedki [1,#], Yu Shen [2,#] and Ashok Mulchandani [2,3*]

[1]Materials Science and Engineering Program, University of California, Riverside, Riverside, CA 92521, USA

[2]Department of Chemical and Environmental Engineering, University of California, Riverside, Riverside, CA 92521, USA

[3]Center for Environmental Research and Technology (CE-CERT), University of California, Riverside, Riverside, CA 92507, USA

# Equal contributions

* Correspondence: adani@engr.ucr.edu

Abstract

Field-effect transistor (FET) is a very promising platform for biosensor applications due to its magnificent properties, including label-free detection, high sensitivity, fast response, real-time measurement capability, low running power, and the feasibility to miniaturize to a portable device**.** 1D (e.g. carbon nanotubes, Si nanowires, conductive polymer nanowires, 1D metal oxides, and others) and 2D (e.g. graphene materials, transition metal dichalcogenides, black phosphorus, and 2D metal oxides) materials, with their unique structural and electronic properties that are unavailable in bulk materials, have helped improve the sensitivity of FET biosensors and enabled detection down to single molecule. In this review, we give insights into the rapidly evolving field of 1D and 2D materials-based FET biosensors, with an emphasis on structure and electronic properties, synthesis, and biofunctionalization approaches of these nanomaterials. In addition, the progress in the 1D/2D-FET biosensors in North America, in the last decade, is summarized in tables. Moreover, challenges and future perspectives of 1D/2D-FET biosensors are covered.

Keywords: 1D materials, 2D materials, field-effect transistor (FET), Nano-FET biosensors.

Table of Content

1. Introduction

A biosensor is an analytical tool that transforms biological events into a measurable output signal. A biosensor consists of three main parts, a biological recognition element or simply a bioreceptor, a transducer, and the associated electronics or signal processor (Baryeh et al., 2017). Based on the type of transducer, biosensors can be stratified into mechanical, optical, electrochemical, electrical, etc (Blair and Corrigan, 2019; Kim et al., 2019; Liao et al., 2019). Mechanical sensors detect events in the form of changes in mechanical properties such as stress or strain on cantilever (e.g. cantilever sensors) or changes in mechanical waves in a piezoelectric material (e.g. acoustic wave sensors) (Zhang and Hoshino, 2014). Optical sensors depend on the change in optical signal utilizing many techniques, including surface plasmon resonance, Raman scattering, fluorescence, and colorimetry (Xu et al., 2020). Electrochemical sensors are a group of sensors that measure the change in current (amperometric), potential (potentiometric), or conductivity (conductometric) as a response to a change in analyte concentration (Hussain and Keçili, 2020; Peixoto and Silva, 2017). On the other hand, electrical sensors rely on detecting the change in electrical signal associated with variation in analyte's concentration and can be classified into field-effect transistors (FET), chemiresistors, chemical diodes, etc (Yao et al., 2021). For each type of these sensors there are strengths and weaknesses, and it all depends on researchers'/users' preferences based on the requirements of each application, available resources and other contributing factors.

FET is very promising for biosensing due to its magnificent properties, including label-free detection, high sensitivity, fast response, real-time measurement capability, low running power, and the feasibility to miniaturize to a portable device. In FET biosensors, bioreceptors are immobilized on a semiconductor channel/sensing material connecting source (S) and drain (D) electrodes. The material interface is a crucial part of the transduction process in FET sensors. A bias voltage is applied on the semiconductor material. The material electronic properties, including electrical conductivity, can be modulated by a third electrode (gate). The captured analytes alter the material conductance, by electrostatic gating or/and Schottky barrier modulation, resulting in a signal that can be recorded and the analyte concentration determined (Y. Chen et al., 2017b; Heller et al., 2008). FET sensors were first operated using bulk materials of metals oxides (e.g. SnO_2) and polymeric membranes as sensing channel materials. However, these bulk materials had unfavourable electronic properties and poor interactions with target analytes limiting their applicability in FET sensors. Moreover, many of these materials function best at high temperature which is not suitable for biosensing (Barsan and Weimar, 2003; Mcbride et al., 1978; Pham et al., 2019). Differently, semiconducting nanomaterials have attracted a huge attention as channel materials for FET biosensors because of their high surface area combined with their nanoscale dimensions that are comparable to the Debye length (λ_D) that

allows for a higher sensitivity (Chartuprayoon et al., 2015; Masurkar et al., 2020).

Among all morphologies of nanomaterials, 1D and 2D semiconducting nanomaterials have been widely implemented in FET sensors. **Fig. 1** shows the 1D and 2D materials used or promising for use in FET biosensors. For 1D semiconductors, silicon nanowires (SiNWs), carbon nanotubes (CNTs), and conductive polymer nanowires (CPNWs) have been materials of choice in FET biosensors. This can be attributed to the sensitivity of the FET sensors implementing them, which can be explained in terms of high current switching characteristics (on/off ratio), high surface-to-volume ratio and similarity of λ_D to the sensing material's diameter (Hangarter et al., 2010; Tran et al., 2020). Furthermore, CNTs have attractive physicochemical properties of tuneable conductivity, from insulative to exceptionally conductive, high thermal and chemical stability, and the ease to immobilize bioreceptors, as well as their high surface area and high current on/off ratio (Yang et al., 2015). However, there are some limitations in the application of these 1D nanomaterials in FET biosensors, such as the difficulty to get pure conductive or semiconductive CNTs instead of getting a mixture of semiconductive/conductive CNTs that impacts their electronic properties, the low carrier mobility and chemical instability of SiNWs that requires surface passivation.

2D nanomaterials, such as graphene (G), reduced graphene oxide (rGO), transition metal dichalcogenides (TMDCs), phosphorenes, and 2D metal oxides are very promising for FET biosensors. Based on their 2D structures, they allow for stronger and more conformal contacts with device electrodes when compared to 1D nanomaterials. In addition, the different thicknesses and dimensions of these 2D nanomaterials can be controlled (Sarkar, 2019). Graphene materials, including graphene itself, graphene oxide, and reduced graphene oxide have attracted a great deal of attention as excellent materials for FET sensors (Y. Chen et al., 2017b; Colombo and Venugopal, 2018; Tsang et al., 2019; Tu et al., 2018). Graphene has an exceptionally high surface area of 2630 m^2/g (Chandran et al., 2017), and a very high carrier mobility of 200,000 $cm^2 V^{-1} s^{-1}$, allowing fast electron transfer (Bolotin et al., 2008). However, graphene-FET biosensors' sensitivity is compromised by its low current on/off ratio due to the absence of intrinsic band gap (Zhang and Lieber, 2016). Other families of 2D nanomaterials have recently been successfully used as alternative semiconductor materials for FET biosensors, such as few-layer TMDCs, black phosphorus (BP) or phosphorene, layered complex oxides, transition metal oxides (e.g. ZnO, In_2O_3, $LaVO_3$, $LaMnO_3$), and hexagonal boron nitride (h-BN) (Bao et al., 2018; Khan et al., 2020; Li et al., 2016; Torrisi and Coleman, 2014; Zhu et al., 2015).

From materials perspective, this review covers the structure and properties, synthesis routes, biofunctionalizations and featured applications between 2010 and 2020 from North America of the 1D and 2D materials used in FET biosensors. In addition, the working principle and sensing mechanism of

nanomaterials-based FET biosensor are explained. Furthermore, the challenges and future perspectives of these materials' synthesis and applications in FET biosensors are discussed.

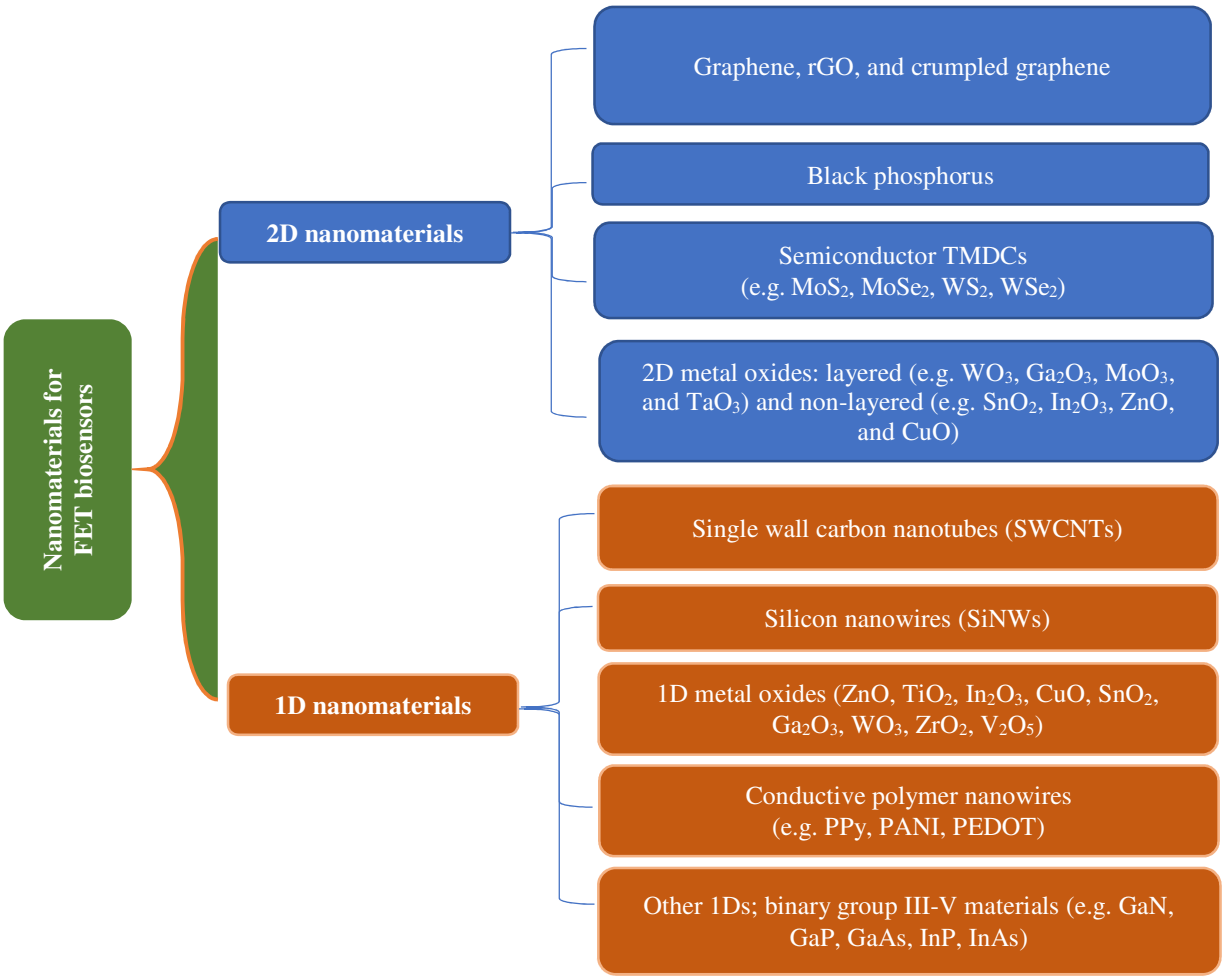

Fig. 1. A schematic chart showing the different 1D and 2D materials used or promising for FET biosensors. SWCNTs: single wall carbon nanotube. PPy, PANI, and PEDOT: polypyrrole, polyaniline, and poly(3,4–ethylenedioxythiophene).

2. Nanomaterial-based FET biosensors

2.1. Operating principles of nanomaterial-based FET biosensors

Fig. 2 (a) depicts the simplest configuration of the FET biosensors that have three electrodes: a source, a drain, and a top/liquid-ion gate. FET biosensors can be top/liquid-, back-, or double-gated. The source-drain conductance of the semiconducting channel can be switched on or off by the gate electrode (Kaisti, 2017). For instance, applying a positive gate voltage on a p-type semiconductor leads to a depletion of carriers and a decrease in conductance, whereas a negative gate voltage leads to an accumulation of carriers and an increase in conductance (Chartuprayoon et al., 2015). On the other hand, chemiresistor

biosensors are a variation of FETs in which the physical gate is replaced with the modulation due to charge adsorbed on the transducer surface. The charged analytes recognized by the bioreceptors near the surface of the semiconductor directly interact with the transducer and impact its electrical characteristics. Electrostatic gating, modulation in carrier mobility, changes in gate coupling and Schottky barrier effects are potential mechanisms for the sensor response. Based on a systematic analysis of each of these mechanisms in the case of SWCNT-based FET biosensors, Heller et al concluded electrostatic gating effect and Schottky barrier modulation were the two dominant mechanisms (**Fig. 2 (b)**). Electrostatic gating refers to the effect that the charges of adsorbed analytes produce upon adsorption on semiconductor leading to doping producing a horizontal shift of the transfer curve (I_{SD}-V_G) due to the Fermi level shifting. Differently, Schottky barrier modulation refers to electrical changes brought by the adsorption of analytes at the contact region between the metal source/drain electrode and semiconductor, which modulates the metal work function and thus the band alignment. Consequently, the current/resistance of the semiconductor is influenced. Since the Schottky barrier heights changes in opposite direction for different charge carriers, i.e., holes (p) and electron (n), the Schottky barrier modulation can be observed by the asymmetric change in the slope of the p- and n- branches of the transfer curve (Heller et al., 2010, 2008).

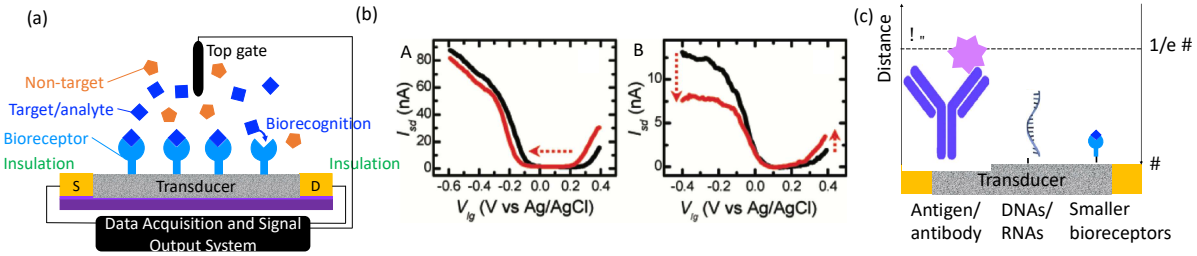

Fig. 2. Schematic diagrams of the FET biosensors structure, functionalization strategies and mechanism (not to scale). (**a**) A schematic illustration of the top-gated FET biosensor structure. (**b**) Modulation of SWCNT-FET transfer curve due to (A) electrostatic gating and (B) Schottky barrier effect. Reprinted with permission from (Heller et al., 2008). Copyright (2008) American Chemical Society. (**c**) A conceptual diagram for the Debye Length (λ_D) and relative size comparison of different bioreceptors and the relative point of observation of biorecognition events.

2.2. Advantages of nanomaterial employment

Recent decades have witnessed an enormous increase in the development of nano-FET biosensors that can be ascribed to the nanomaterials employment, including nanowires, nanotubes, nanosheets and other 1D and 2D nanostructures. In the U.S., this can be attributed to the launching of the National Nanotechnology Initiative program in the year 2000 by the federal government. 1D nanomaterials with high aspect ratios have 1D quantum confinement, hence the charge carriers do not shunt around the interaction zone, and thereby lead to larger depletion/accumulation of the charge carriers deep into the entire 1D semiconductor, compared to the

planar sensors (Chartuprayoon et al., 2015). For 2D nanomaterials, their large surface area, high carrier mobility, high mechanical strength, the flexibility of doping, and phase transformation make them ideal for FET biosensors. Furthermore, the large lateral size of 2D nanosheets provides consistent contacts with S-D electrodes and thus reduces the device variations (Bhimanapati et al., 2015). In addition, the large surface areas of nanomaterials enable the super sensitivities and rapid response time via direct conversion of the recognition event into electrical signals.

Recently, another study investigated the origin of the improved sensitivity of nanomaterial-based biosensors (Shoorideh and Chui, 2014). The study concluded that the improved sensitivity of nano-sized FET is from the nanoscale geometries instead of FETs that are simply scaled down. The miniaturized concave surfaces experience a weaker counter-ion screening effect and therefore show a higher sensitivity to the change in surface charges than convex surfaces, and the sensitivity improves as the wire radius approaches the λ_D (Shoorideh and Chui, 2014). As a result, FET biosensors employing nanomaterials show superior performances; although these nanomaterials themselves maybe convex-shaped, they can form a large number of concave corners by lying on the substrate or forming a network, which offers an alternative explanation to the improved sensitivity of nanoFET biosensors.

The sensitivity of FET biosensors is also impacted by the λ_D, which is defined as the distance from the solid-liquid interface to the boundary between the diffuse layer and bulk solution. λ_D is important since it describes the penetration depth of the electrical field due to the adsorbed surface charge into the semiconductors—and is regarded as the "minimum sensing distance" (**Fig. 2 (c)**). At the point of observation at one λ_D, the electrical signal decay to 1/e (Israelachvili, 2011; Kaisti, 2017). Thus, nanomaterials exhibit great benefits in providing nanoscale features that approach the λ_D of commonly seen physiological solutions.

2.3. Strategies to improve sensitivity of nano-FET biosensors

Besides the enhanced surface area of the FETs biosensors employing nanomaterials, there are other factors that could improve the sensitivity. First, to eliminate the electrostatic screening and decay in electrical responses, solutions with low ionic strength are preferred due to larger λ_D. However, practical samples often contain high concentration of interferents, such as high concentration of salts in clinical blood samples, and thus it is unrealistic to expect low ionic strength in physiological samples. Therefore, bioreceptors with smaller sizes, such as aptamers, ssDNA/RNA, antibody fragments, peptides, have been reported to ensure the biorecognition within the λ_D to improve the sensitivity (Ahn et al., 2011; Cheng et al., 2014; Elnathan et al., 2012; Gao et al., 2020; Kim et al., 2008; Wang et al., 2019). Moreover, the length of the linkers used in the bioreceptor conjugation also increase the distance from the interface (Kaisti, 2017). Therefore, using smaller

linkers would help gain higher sensitivity. Furthermore, Li et al. studied the effect of the number, doping, and diameter of nanowires on the biosensing sensitivity and found that single NW with lower doping density and smaller diameter showed improved sensitivity than multi-NW FET (Li et al., 2011). Lastly, to mitigate the screening effect, high frequency alternating currents can be employed to produce mixing currents that are highly sensitive to the change in surface charges at 100 mM buffer (Kulkarni and Zhong, 2012). Taken together, nanomaterial-based FETs are able to detect analyte on a single molecule level and show tremendous potential in fabricating highly sensitive, highly selective biosensors.

3. 1D nanomaterials-based FET biosensors: structure and properties, synthesis, biofunctionalization and featured applications

3.1. Carbon nanotubes

3.1.1. Structure and properties

CNTs can be regarded as one or more graphene sheets that are "rolled-up" into seamless tubes of nanometer diameter and are divided into single-walled carbon nanotubes (SWCNTs) and multi-walled carbon nanotubes (MWCNTs). In graphite, sp^2 hybridization occurred in the x-y plane where each carbon atom is connected to three carbons at 120° with a bond length of 1.42 Å; whereas the π-bond exist in the z axis with free electrons moving in the P_z orbital to give high conductivity. Similarly, the concentric layers of CNTs have an interlayer spacings of ~ 3.4 Å (close to the that of graphite: 3.35 Å) (Jariwala et al., 2013; Lan et al., 2011). As shown in **Fig. 3 (a)**, the different rolling angles result in different chirality of SWCNTs: two vectors ($n\vec{a}_1$ and $m\vec{a}_2$) describe the chirality of CNTs based on the orientation of the tube axis versus the hexagonal lattice: chiral (n≠m), armchair (n=m), and zigzag (m=0). The electronic properties of CNTs are governed by their structures (i.e., the chiral indices). The different structures of CNTs results in different electronic properties due to the quantum confinements of electrons in the radial direction between CNTs. Depending on chiral indices, the electronic structures of the CNTs can be metallic (n-m = 3k, where k is an integer) or semiconducting (n-m ≠ 3k). MWCNTs are usually considered as metallic since they are highly prone to have at least one metallic shell (**Fig. 3 (c)**) (Nessim, 2010). The typical diameter of SWCNTs is in nanometers. For MWCNTs, the typical inner diameter is sub-nm to a few nanometers, while the outer diameter varies from 2 to 30 nm (Eatemadi et al., 2014). The length of CNTs varies from 100 nm to a few centimeters (De Volder et al., 2013). Therefore, CNTs have a very high aspect ratio and expose large surface areas (50 to 1315 m^2/g) to the environment (Peigney et al., 2001). Other superior physical properties include high electrical conductivity (~ 10^7 S/m), high thermal conductivity (~ 3500 W/mK), ampacity up to 10^{13} A/m^2, and high elastic modulus (> 1 Tpa) (Zhang et al., 2020). Taken together, these interesting properties make CNTs a very suitable nanomaterial for building nano-FETs.

3.1.2. Synthesis of CNTs

Common methods of CNTs production include arc-discharge (AD), laser ablation (LA), and chemical vapor deposition (CVD). AD was first reported by Iijima in 1991 and is one of the most widely used methods to grow CNTs (Iijima, 1991) AD requires a high temperature (> 1700 ˚C) and utilizes metal catalysts between high-purity graphite electrodes in a pressurized chamber with evaporated carbon molecules. Currents pass through the chamber during arching as the carbon deposits at the cathode tip and chamber wall to form carbon soot. SWCNTs and MWCNTs are synthesized in the inner core of the soot. The proper choices of catalyst precursor-graphite mixture enhance the selective yield of SWCNTs, such as Ni-Y-graphite mixtures (Eatemadi et al., 2014). However, AD has less control on the purity and uniformity of the CNTs. Thus, it requires further purifications, which uses strong acids that may shorten CNT length and introduce more surface defects and eventually affect the electronic properties (Ramnani et al., 2016). LA was first introduced as an alternative to the AD (Guo et al., 1995). It uses a high-power laser to vaporize the graphite at high temperature (1200 ˚C). Similar to AD, LA requires metal catalysts, such as cobalt and nickel. LA method produces CNTs with high purity and quality, however, the high energy consumption and expensive instrument limit its commercialization. The CVD method uses a metal catalyst, usually nickel or cobalt. In a CVD method, a carbon-containing gas, such as ethylene or acetylene, and a carrier gas, such as nitrogen, are loaded to the reactor, where the silicon substrate is templated with implantation for CNT growth. The carbon-containing gas is believed to be broken into carbon atoms at the surface of the catalyst surface to generate CNTs (Bhushan et al., 2014). CVD has gained more popularity for high-volume production with high structural control at lower temperature (< 800 ˚C) although with more defects than AD and LA production. However, CVD is advantageous in allowing direct CNTs growth on substrates and mass production that requires low cost and simple instrument (Rashid and Ralph, 2017). The as-synthesized CNTs are usually mixtures of carbonaceous impurities, metal catalysts, semiconducting and metallic CNTs with varying dimensions and morphologies, which require further purification before their use in FET biosensors. Typically, the purification involves the removal of bulk graphite particles and aggregates by harsh treatments, dissolution of metal catalysts, removal of carbon clusters, and separation of semi- and metallic-CNTs. In addition, to avoid CNT bundle formation due to the van der Waals (vdW) forces, chemical oxidation, surfactants and sonication are employed to suspend CNTs in solution. The Hersam group employed density gradient ultracentrifugation for separating SWCNTs on the basis of diameter, electrical property, (*n,* m) structures, enantiomer sorting and even handedness (Arnold et al., 2006, 2005; Green et al., 2009; Green and Hersam, 2009). Purified CNTs, such as purified semiconducting SWCNTs, show superior properties suitable for FET biosensors, including high field-effect mobility, high intrinsic carrier mobility, and high on/off ratios (Bati et al., 2018; Ramnani et al., 2016).

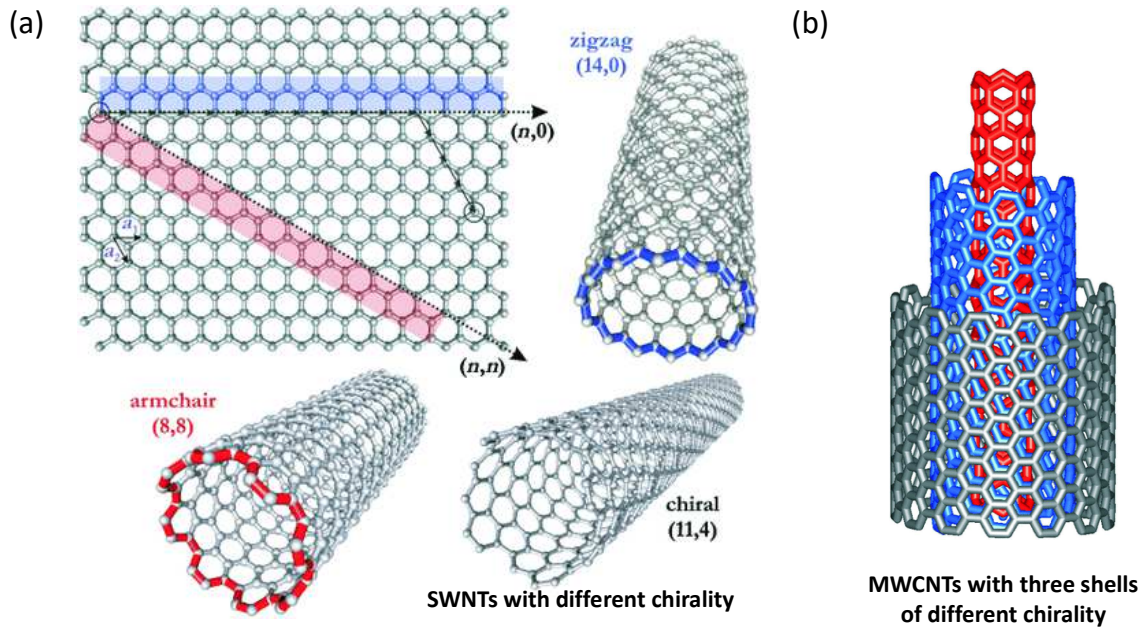

Fig. 3. Structure of CNTs with various chirality. (a) Molecular models of SWCNTs exhibiting different chirality: armchair, zig-zag, and chiral conformations. (b) Structure of an MWCNT made up of three shells of differing chirality. Adapted with permission from (Balasubramanian and Burghard, 2005). Copyright (2005) WILEY-VCH Verlag GmbH & Co. KGaA, Weinheim.

3.1.3. Biofunctionalization strategies and biosensor applications

CNTs are rolled graphene sheets, and hence their covalent functionalization is similar, and readers are directed to Section 4. In addition, non-covalent aromatic-like linker functionalization includes wrapping with surfactant (Karajanagi et al., 2004; Kwon et al., 2013; Moore et al., 2003), polymer (Fennell et al., 2017; Mago et al., 2009; O'Connell et al., 2001; Star et al., 2001) and DNA (Xu et al., 2007; Zheng et al., 2003). In addition, direct adsorption is also employed for straightforward functionalization (Gong et al., 2019; Mao et al., 2010). Among all, the non-covalent functionalization of linkers on CNTs is of great interest since it does not introduce defects and maintains their electrical and mechanical properties, while providing active moieties for bioconjugation (Chen et al., 2001; Simmons et al., 2009; Zhou et al., 2019).

The fabrication of CNT-based FET biosensors evolves from single SWCNT patterning between source and drain electrodes (Kong et al., 2000), to dielectrophoretic aligning on pre-fabricated microelectrodes (Tlili et al., 2011), to self-assembled monolayer of CNT network on pre-fabricated microelectrodes (Ramnani et al., 2016; Wang et al., 2009), and bulk deposition of CNT networks by vacuum filtration, screen printing, and inkjet printing (Kholghi Eshkalak et al., 2017; Lei et al., 2015; Medina-Sánchez et al., 2014; Shen et al., 2019; Taleat et al., 2014). Furthermore, CNT-based composites with metal nanoparticles are drawing

attention in the FET biosensors community (Shao et al., 2019; Silva et al., 2017). **Table 1** summarized the development of employing CNTs in FET biosensors in North America. These ultrasensitive and selective FET biosensors based on functionalized CNTs have been widely applied to various scenarios, such as disease diagnosis, environment monitoring, food safety, and agriculture.

Table 1. Summary of recently developed CNT-based FET biosensors by North American institutes since 2010

1D nanomaterial	**Bioreceptor**	**Analyte**	**LOD**	**Linker**	**Ref.**
Single SWCNT	Antibody	Horseradish peroxidase	~ 10^{-6} mol/L	Linker-free adsorption	(Mao et al., 2010)
SWCNTs	Antibodies	*E. coli O157:H7* and bacteriophage T7	10^5 CFU-*E. coli O157:H7*/mL; 10^2 PFU-T7 phage/mL	PBASE	(García-Aljaro et al., 2010b)
SWCNTs	Oligonucleotide probe-anti-ATP aptamer hybrid	ATP	1 pM	PBASE	(Das et al., 2011)
SWCNTs	Porphyrin-based glycoconjugates	Lectins (PA-IL, PA-IIL and Concanavalin A)	2 nM	Linker-free adsorption	(Vedala et al., 2011)
SWCNTs	Antibody	Cortisol	0.11 pg/mL	1-Pyrenemethylamine hydrochloride	(Tlili et al., 2011)
DNA/SWCNT NWs	DNA probe	DNA	10 fM	Covalent bond with SWCNTs	(Weizmann et al., 2011)
CNTs	Antibody fragment	Prostate cancer biomarker OPN	30 pM	Covalent bond with SWCNTs	(Lerner et al., 2012)
CNTs	DNA probe	E. coli *O157* DNA	1 pg/mL	Covalent thiolation	(Subramanian et al., 2012)
SWCNTs	Antibody	Lyme flagellar antigen	0.1 ng/mL	Covalent bond with SWCNTs	(Lerner et al., 2013)

SWCNTs/GO	Biotin	Avidin	-	AuNP decoration	(Chang et al., 2013)
SWCNTs	MicroRNA probe	miRNA-122a	1 aM	PBASE	(Ramnani et al., 2013)
AuNP decorated SWCNTs	Pyrene-biotin	CaptAvidin	-	Pyrene-biotin	(Münzer et al., 2014)
SWCNTs	Antibody	Microcystin-L	0.6 ng/L	PBASE	(Tan et al., 2015)
SWCNTs	polyT:polyA duplex	Salivary mercury	1 nM	PBASE	(Wordofa et al., 2016)
SWCNTs	Heparin	Dengue virus	8.4×10^2 $TCID_{50}$/mL	1-Pyrenemethylamine	(Wasik et al., 2017)
SWCNTs	Dodecanethiol lipoic acid	Murine tissue cells	-	AuNP decoration	(Silva et al., 2017)
SWCNTs	Concanavalin A lectin	*Escherichia coli K12*, *Enterococcus faecalis*, *Streptococcus mutans*, and *Salmonella typh*	4.7×10^3 cfu/mL, 25 cfu/mL, 7.4×10^4 cfu/mL, and 6.3×10^2 cfu/mL, respectively.	PBASE	(Saucedo et al., 2018)
SWCNTs	Antibody	Dengur virus NS1 protein	1 ng/mL	PBASE	(Wasik et al., 2018)
SWCNTs	Calmodulin	Ca^{2+}	10^{-15} M	AuNP decoration	(Shao et al., 2019)
SWCNTs	SocA	Fructosyl valine	1.2 nM	PBASE	(Hatada et al., 2019)
SWCNTs	Antibody	Human serum albumin	1 pM	1-pyrene carboxylic acid	(Shen et al., 2019)
SWCNTs	red blood cell membrane	Broad-Spectrum Hemolytic Toxins; acterial Whole	fM range	Linker-free adsorption	(Gong et al., 2019)

		Secreted Proteins			
SWCNTs	Antibody	Huanglongbing biomarker SDE1	5 nM	PBASE	(Tran et al., 2020)

3.2. Conducting polymer nanowires

3.2.1. Structure and properties

Conducting polymer nanowires (CPNWs) have been a backbone nanomaterial in biosensing technology due to their excellent electronic and mechanical properties. Common CPs include polypyrrole (PPy), polyaniline (PANI), and poly(3,4–ethylenedioxythiophene) (PEDOT). The molecular structures common CPNWs and SEM images PPy, PANI, PEDOT-based FET are shown in **Fig. 4**. CPNWs are repeat sequences of monomers with sp^2 hybridized backbones. For instance, PANI is a homopolymer existing in different oxidative states depending on the synthesis procedure and the doping extent. Pristine CPNWs are insulators or semiconductors and require additional dopants to improve their conductivity, charge carrier density, and tertiary structures. Moreover, the differences in CP chain lengths, chain alignments, molecular weights, grain boundaries, crystallinity, surface area, and other structural features also affect their properties (Hangarter et al., 2010). Furthermore, the synthesis method affects their physical and chemical properties, such as the disorder of CPNWs ranges from disordered, semi-crystalline with non-conductive peripheries, to crystalline structures with high electrical conductivity. (Long et al., 2011). Moreover, as the dimensions of CPNWs decrease, the physical and chemical properties are significantly changed and provide advantages for the application in FET biosensors because the size reduction increases the surface area and shorter transport path of analyte to the wire surface. CPNWs also show excellent electronic conductivity over a wide range from 10^{-3} to 10^3 S/cm, depending on the dopant type and level (Long et al., 2011). On the other hand, PEDOT has poor aqueous solubility but can be mitigated by combining poly (styrene sulfonic acid) (PSS) as the charge-balancing dopant during polymerization of PEDOT:PSS (Park et al., 2016).

3.2.2. Synthesis of CPNWs

Methods to synthesize CPNWs can be classified into template and template-free (Bangar et al., 2010). Template methods include hard-template, soft-template, and nanostructure-template. Hard templates utilize anodic aluminum oxide (AAO), zeolites, methyl orange, porous silica, and TiO_2 nanotube arrays. Synthesis using soft and nanostructure-based templates, such as CNTs, have additional benefits of both serving as the

template and the doping agent, eliminating the template removal step. Soft templates include gelatins, starch, adenosine triphosphate (ATP), anthraquinone-2-sulfonic acid sodium (AQS) and p-toluenesulfonyl sodium (Bach-Toledo et al., 2020). To fabricate CPNWs into biosensors, however, these approaches have a few downsides: they

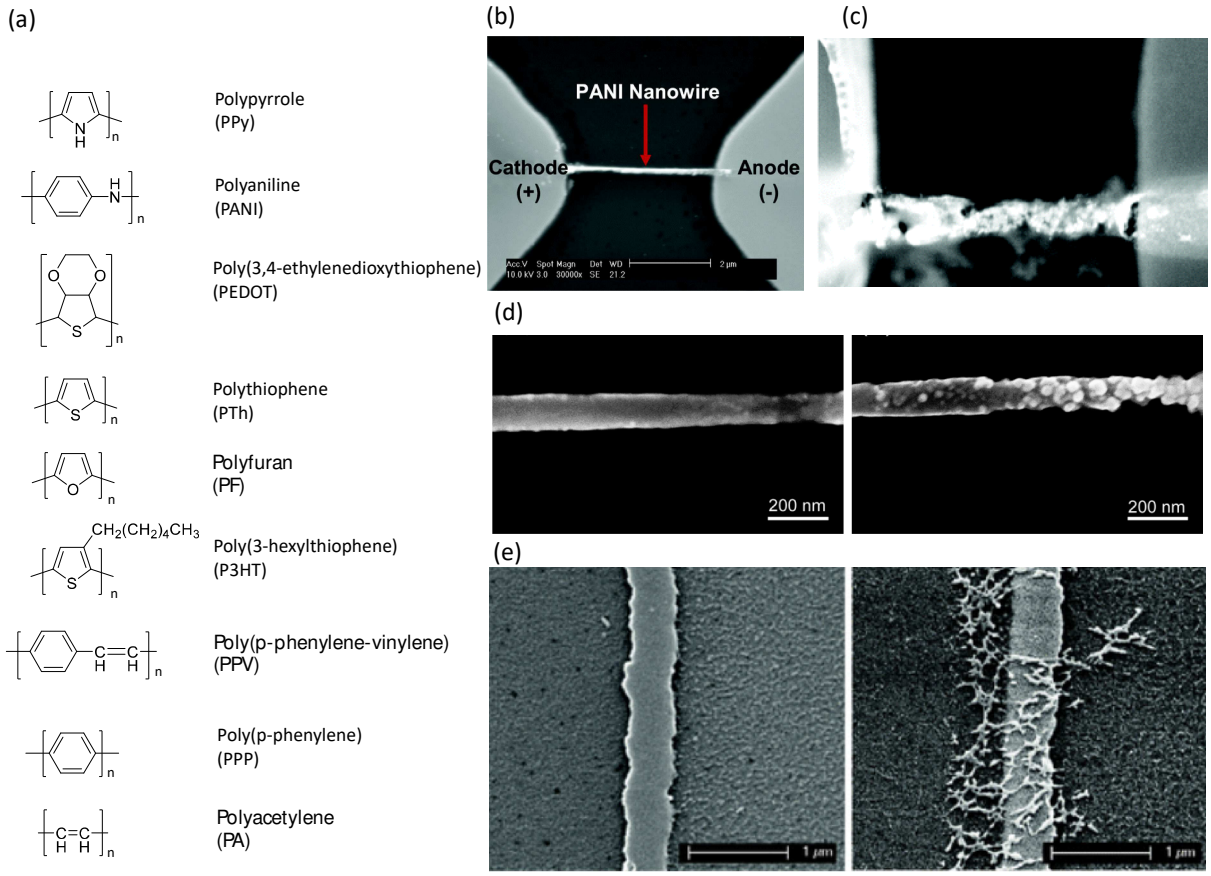

Fig. 4. Molecular structures of common CPNWs and some of their SEM images. (a) Molecular structure of common conducting polymers. (b) SEM image of a 100 nm wide by 4 μm long PANI nanowire. Scale bar: 2 μm. Reprinted with permission from (Ramanathan et al., 2004). Copyright (2004) American Chemical Society. (c) SEM image of a single avidin-conjugated ZnSe/CdSe quantum dots-embedded PPy nanowire (200 nm wide). Reprinted with permission from (Ramanathan et al., 2005). Copyright (2005) American Chemical Society. (d) SEM images of of single PANI NW before (left) and after (right) functionalization with monoclonal antibodies. Adapted from (Lee et al., 2012). (e) SEM images of single PEDOT NWs (left) and net-like structure of virus-PEDOT composite (right). Reprinted with permission from (Arter et al., 2012). Copyright (2012) American Chemical Society.

usually use harsh chemicals, require alignment after synthesis, and multiple steps for functionalization. To overcome the drawbacks, one-step approaches of composite CPNWs with bioreceptors produce nanowires for direct fabrication into biosensors. Individual PANI NW between electrodes with well-controlled dimension and high aspect ratio has been synthesized by an electrodeposition method (**Fig. 4 (b)**) (Ramanathan et al., 2004). Ramanathan et al. later employed it for entrapping a model protein, avidin, during

the one-step polymerization of PPy NW (**Fig. 4 (c)**). The *in situ* synthesis integrated the biorecognition molecules during the PPy polymerization, eliminating the post-synthesis alignment and functionalization (Ramanathan et al., 2005). Furthermore, Arter et al. developed a lithography patterned nanowire electrodeposition (LPNE) method to synthesize linear arrays of virus-PEDOT NWs (Arter et al., 2010). Photolithography was used to pattern trenches in the photoresist layer on a nickel film-coated glass, followed by a crucial step of oxidation and the removal of the exposed nickel. These nano-trenches with nickel on both sides served as the electrodeposition cell for growing PEDOT NWs that were directly applied for FET biosensing. On the other hand, template-free methods utilizes a driving force for guiding the interfacial polymerization. Among all, simple and cost-effective electrochemical synthesis of PANI NWs was employed for direct production and fabrication of PANI NW network between S-D electrodes (Van Tuan et al., 2012; J. Wang et al., 2004). Zhang et al. developed a template-free approach to synthesize PPy nanofibers with catechol derivatives. The dopamine (DA)-functionalized PPy nanofibers had a fibrous morphology and showed the highest electrical conductivity (3.8 S/cm for DA-PPy pellet and 1.1 S/cm for DA-PPy film), while the pristine PPy was granular and showed low conductivity (0.04 S/cm for PPy pellet and 0.01 S/cm for PPy film). The catechol moieties also improved its water dispersibility, interfacial adhesion, and provided chemically reactive pathways for bioconjugations (W. Zhang et al., 2015). Furthermore, facile patterning methods, such as inkjet printing of CPNWs ink, are drawing great attention recently (Song et al., 2015).

3.2.3. Biofunctionalization strategies and biosensor applications

Table 2 summarizes the CPNW-based FET biosensors developed in recent 10 years by North American researchers. For instance, the **-**NH_2 groups of NWs can be crosslinked with -COOH groups of the bioreceptors via the formation of an amide bond via carbodiimide chemistry. Lee et al. used such functionalization chemistry to immobilize antibodies on the PANI-NW covalently for the detection of cardiac biomarkers at fg/mL level (**Fig. 4 (d)**) (Lee et al., 2012). Another functionalization strategy uses linker molecules such as succinimidyl 4-[p-maleimidophenyl]butyrate (SMPB) that contains a N-hydrosuccinimide ester (NHS) on one end to bind to an amine and a maleimide group at the other end to bind sulfhydryl group. Bangar et al. used SMBP linker to functionalize a single PPy NW with ssDNA probe to hybridize with the target ssDNA down to ~100 aM (Bangar et al., 2011). In addition, the bioreceptors can be anchored/embedded before the polymerization. Penner and coworkers have dedicated to the development of virus-polymer hybrid-based FET biosensors, in which the virus particles were embedded into PEDOT NWs during the electrodeposition as the recognition element (**Fig. 4 (e)**)(Arter et al., 2012). This work paved the way for a series of biosensors based on PEDOT nanostructures embedded with virus particles (Bhasin et al., 2020, 2018; Mohan et al., 2013; Ogata et al., 2017).

Table 2. Summary of recently developed CPNW-based FET biosensors in North American institutes since 2010.

1D nanomaterial	Bioreceptor	Analyte	LOD	Linker	Ref.
PPy NWs	antibody	*Bacillus globigii*	1 CFU/mL	Covalent bond with PPy NWs	(García-Aljaro et al., 2010a)
single PPy NW	antibodies	Bacteriophages (T7 and MS2)	10-3 PFU	Covalent bond with PPy NW	(Shirale et al., 2010)
single PPy NW	ssDNA probe	ssDNA	100 aM	SMPB	(Bangar et al., 2011)
virus-PEDOT NWs	PSMA-3	PSMA	56 nM	Virus embedded in PEDOT NWs	(Arter et al., 2012)
single PANI NW	antibody	Cardiac biomarkers (Myo, cTnI), CK-MB, and BNP)	100 pg/mL for Myo, 250 fg/mLfor cTnl, 150 fg/mL for CK-MB, and 50 fg/mL for BNP	Covalent bond with PANI NW	(Lee et al., 2012)

3.3. Silicon nanowires

3.3.1. Structure and properties

SiNWs usually grow with random directions and diameters, however, the techniques to synthesize SiNWs with controlled structures are reviewed later. As shown in **Fig. 5 (a & b)** there are five general classes of controlled structures for SiNWs: basic/homogeneous, axial modulated, radial/core-shell modulated, branched, and kinked structures (Zhang and Lieber, 2016). Homogeneous SiNWs are a type of nanomaterial that has a uniform composition with a typical diameter of 3 - 500 nm and a typical length in nanometers to millimeters. For forming the axial heterostructure, the metal catalyzes the continuous SiNW growth with different vapor reactants. Radial/core-shell SiNWs are formed by the shell NW deposition on the core NW. Branched SiNWs refer to the SiNWs with tree-like heterostructure. Kinked SiNWs have two straight arms with a fixed angle at the joint point (Zhang and Lieber, 2016).

The electronic properties of SiNWs are influenced by their growth orientation, diameter, morphology, surface

modification, doping, and alignment. For example, the SiNW bandgap width is inversely proportional to the diameter (Mohammad, 2014; Yan et al., 2007). The charge mobility of SiNWs is another important electrical property in FET sensors. Theoretical calculations and experimental works have revealed some of the relationships between the charge mobility and SiNWs synthesis and structures (Ramanujam et al., 2011). Lieber group reported multiple advances in the controlled structures and enhanced properties of SiNWs by varying diameters, doping, enhanced charge mobilities (Duan and Lieber, 2015). Carrier mobility were improved from doping, thermal annealing and the passivation of the oxide defects. (Cui et al., 2000). p-type SiNWs with smaller diameter of 20 nm demonstrate higher charge mobility up to 10^3 $cm^2V^{-1}s^{-1}$, although the enhanced mobility was ascribed to the induced strain due to the oxide layer of the SiNWs. Even smaller SiNWs with diameter of about 5 nm show high hole and electron mobility of about 325 $cm^2V^{-1}s^{-1}$ and 750 $cm^2V^{-1}s^{-1}$ with the two-step annealing process (Ramanujam et al., 2011). Besides, the high on/off ratios and low leakage currents are favored in the FET biosensors. Therefore, by controlling the doping level, surface morphology, dimensions and orientations of the SiNWs, the electronic properties can be tuned.

3.3.2. Synthesis of SiNWs

SiNWs are fabricated with two mainstream methods: (1) top-down lithography that provides accurate, uniform, and flexible SiNWs synthesis and alignment, and (2) bottom-up approach that achieves good scaling-down fabrication (Penner, 2012). The top-down method usually uses a combination of patterning, photolithography, deposition, and chemical etching to fabricate nanoscale sensing channels on a substrate. Bottom-up method, on the other hand, is based on vapor-phase growth to synthesize desired nanostructures building on individual atoms and molecules with tunability of NW lengths. Many bottom-up approaches have been reported, such as vapor-liquid-solid method (VLS), oxide-assisted growth, photolithography, and e-beam lithography (Ramanujam et al., 2011). The VLS is the most common bottom-up synthesis method. It uses a nanometer-sized catalyst to form a eutectic alloy at the vapor-liquid interface, in which vapor serves as the Si source, allowing Si atom addition at the liquid-solid interface for SiNW growth. Another potent bottom-up synthesis of SiNW is CVD-VLS to synthesize well-controlled nanowires. It uses a gas precursor as the Si source, such as SiH_4 or $SiCl_4$, carried to the catalyst in the Ar or H_2 atmosphere for the orientated growth of SiNWs (Zhang and Lieber, 2016). An interesting paper-like fabric comprised of crystalline SiNWs was fabricated. The SiNWs had diameters ranging from 10 to 50 nm and an average length larger than 100 mm. By dropcasting the concentrated SiNW/toluene dispersion on a Teflon trough, the fabric of highly entangled SiNWs was formed (Chockla et al., 2011). For building a SiNW FET, Au electrodes are commonly used as the source and drain electrodes, with the synthesized SiNWs bridging in-between, while the bulk Si substrate separated by a SiO_2 layer is used as a global back gate.

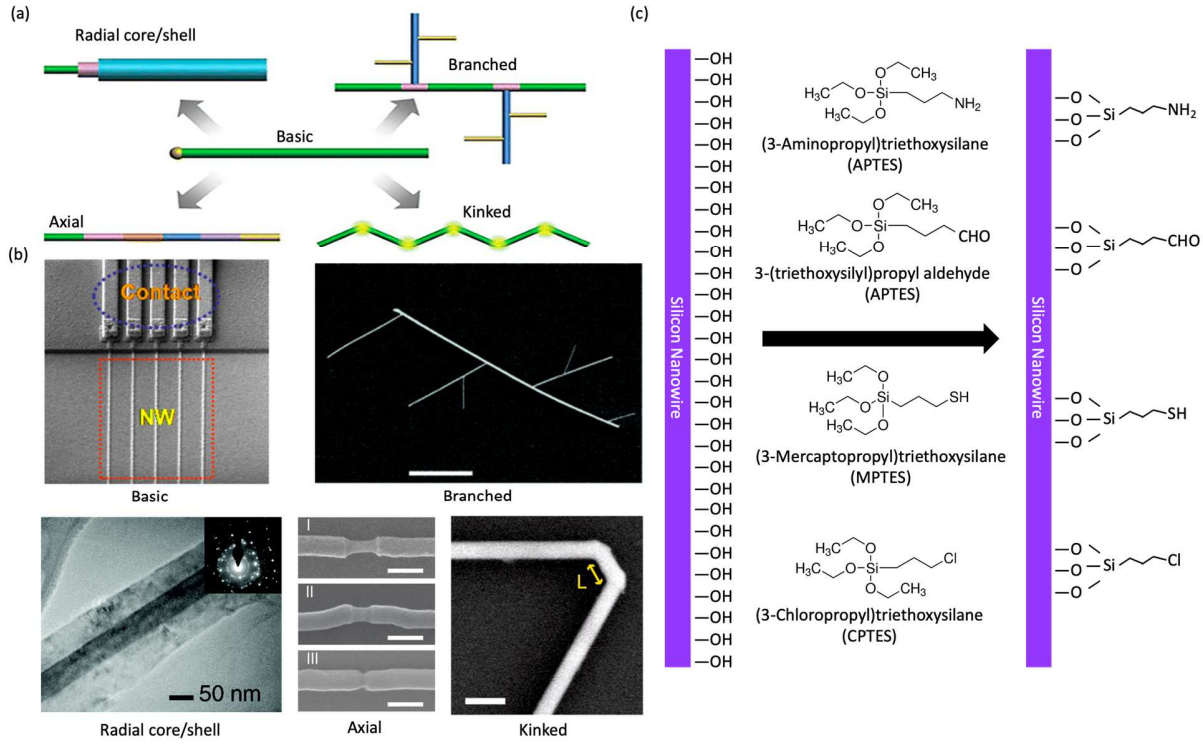

Fig. 5. Structures of SiNWs and biofunctionalization strategies. (a) Five structures of SiNWs. Reprinted with permission from (Zhang and Lieber, 2016). Copyright (2016) American Chemical Society. (b) SEM or TEM images of the five structures of SiNWs. Scale bars are: 500 nm (axial), 200 nm (kinked), 500 nm (radial core/shell), and 1 μm (branched). SEM of the basic SiNW is reprinted from *Sensors and Actuators B: Chemical* 146: 138-144 (Zhang et al., 2010). Copyright (2010), with permission from Elsevier. SEM of the axial SiNW is reprinted with permission from (Cohen-Karni et al., 2012). Copyright (2012) American Chemical Society. SEM of the kinked SiNW is from (Tian et al., 2010). Reprinted with permission from AAAS. TEM of the radial core/shell SiNW is reprinted with permission from (Garnett and Yang, 2008), Copyright (2008) American Chemical Society. SEM of the branched SiNW is reprinted with permission from (D. Wang et al., 2004). Copyright (2004) American Chemical Society. (c) some common surface modifications of SiNW for biofunctionalizations.

3.3.3. Biofunctionalization and applications to FET biosensors

Silanization is the most common approach to form a self-assembled monolayer for anchoring bioreceptors on silica surfaces (**Fig. 5 (c)**). The covalent functionalization of bioreceptors on SiNWs includes using organosilane such as 3-aminopropyltriethoxysilane (APTES) to introduce amine groups (Li et al., 2011; Liang et al., 2014), 3-mercaptopropyltriethoxysilane (MPTES) to introduce thiol groups (Li et al., 2005), 11-(triethoxysilyl) undecanal to introduce hydro carbonyl groups (Tian et al., 2011), and 3-(trimethoxysilyl)propyl aldehyde (APTMS) to introduce aldehydes (Zheng and Lieber, 2011). Other methodologies to functionalize silicon surfaces include the use of HF to introduce hydrogen terminations for the attachment of alkyne or alkene monolayer via Si-C bonding. The hydrocarbon monolayer can be further treated under UV radiation to introduce amine groups for bioconjugation with bioreceptors (Bunimovich et

al., 2006).

Since Lieber and coworkers first reported the functionalized SiNWs as chembio-sensors (Cui et al., 2001), a myriad of biosensors have been fabricated using SiNWs (Sang et al., 2016; Tran et al., 2018; Zhang and Ning, 2012). **Table 3** summarized the contributions of FET biosensors employing SiNWs by North American researchers in recent 10 years.

Table 3. Summary of recently developed SiNW-based FET biosensors in North America since 2010.

1D nanomaterial	Bioreceptor	Analyte	LOD	Linker	Ref.
SiNW	Antibody	Prostate specific antigen	0.15 pM	APTMS	(Zheng et al., 2010)
SiNWs	Antibody	Human Immunoglobin G	10 fg/mL	APTES	(Li et al., 2011)
SiNWs	Antibody	Bovine serum albumin	0.1 fM	11-(Triethoxysilyl) undecanal	(Tian et al., 2011)
SiNW	-	Intracellular signal	-	-	(Jiang et al., 2012)
SiNW	(1) HMGB1 (2) Biotin	(1) DNA (2) Streptavidin	-	-	(Duan et al., 2012)
SiNW	ssDNA	miRNA-10b	1 fM	100 fM – 1 μM	(Dorvel et al., 2012)
multi-SiNWs	Antibody	Insulin	10 fM	10 fM – 100 pM	(Regonda et al., 2013)
	Antibody fragments	Melanoma biomarker (TNFRSF19)	200 pM	-	(Maedler et al., 2016)

3.4. Other 1D nanomaterials

3.4.1. Structures and properties

Other 1D nanomaterials to fabricate nano-FET biosensors include metal oxides (ZnO, TiO_2, In_2O_3, CuO,

SnO_2, Ga_2O_3, WO_3, ZrO_2, V_2O_5, etc.) and binary group III-V materials (GaN, InP, GaAs, etc.) and their alloys, such as AlGaN (**Fig. 6 (a)**). Metal oxides can be synthesized as layered or non-layered 2D materials (thin films). Crystal structure and properties of metal oxide nanomaterials are discussed in more details in section 4.3. III-nitride nanowires (III-N NWs) have a wurtzite or cubic structure; the wurtzite is thermodynamically more stable and is employed more regularly (Zhao et al., 2015). III-N NWs grown on non-lattice matched substrate, such as Si, SiC, and sapphire, often show lattice mismatch between the non-native substrate and the III-V layers. Bulk native substrates, herein, are employed to avoid mismatching and increase the crystal quality by reducing the dislocation density and mechanical strain (Kirste et al., 2015).

Owing to their excellent properties, such as high carrier mobility, high on/off ratios, transparency, flexibility, etc., these 1D nanomaterials have found wide applications in biosensing. For instance, ZnO is an n-type semiconducting material with wide bandgap, between 3.1 and 3.4 eV, and a high isoelectric point (IEP ~ 9.5). The former makes it suitable for building FET biosensors, while the latter aids in high loading of bioreceptors with low IEP via electrostatic interaction (Davis et al., 2019; Shanmugam et al., 2017; Xu and Wang, 2011). Similarly, nanowires and nanoribbons of In_2O_3 are promising candidates for FET biosensing applications due to their high surface area that provides abundant loading of bioreceptors, high electronic conductance and high transparency to visible light (Li et al., 2003; Liu et al., 2018). GaN is a semiconducting material with wide bandgap and biocompatibility for specific and sensitive biosensing (Chen et al., 2011; Sahoo et al., 2013). Due to the high bond strength, GaN NWs show high stability in complex environment such as blood (Kirste et al., 2015).

3.4.2. Synthesis of other 1D nanomaterials

The top-down method produces highly uniform nanostructures with outstanding electronic properties, however, it cannot suffice the need for nanomaterials with smaller sizes. On the other hand, the bottom-up approach assembles the 1D nanostructures based on the pre-synthesized building blocks to fabricate smaller nanostructures beyond the limits of the top-down methods. CVD and hydrothermal methods are the most commonly used bottom-up methods via VLS mechanism. Single- and multi-component metal oxide NWs such as ZnO, SnO_2, In_2O_3, Zn_2GeO_4, and $In_2Ge_2O_7$, can be synthesized through this method. Compared to the gas-phase VLS synthesis, solution phase-based (solution-liquid-solid, SLS) approaches show advantages of systematic control of nanowire diameter at the quantum confinement regime, surface passivation, and nanowire solubility. However, they lack the control in nanowire crystal structure and growth direction (Dasgupta et al., 2014). Yang's group synthesized GaP NWs in a SLS-based and organic surfactant-free method. The precursors (triethylgallium and tris(trimethylsilyl)phosphine) were reacted in solvent squalene in a self-seeded manner (Sun et al., 2011). Moreover, microfluidic-based synthesis of nanowires is emerging

and was demonstrated with easy control of nanowire growth parameters (Laocharoensuk et al., 2013). Besides, Liu et al. devised a scalable and facile fabrication of n-typed In_2O_3 nanoribbons of 25 μm wide, 500 μm long and ~ 16 nm thick by a simple RF sputter-coating of In_2O_3 on the masked substrate to make (Liu et al., 2016). The nanoribbons showed a high on/off ratio of 10^7. However, this method is limited to micron level planar dimensions due to the poor mask resolutions.

3.4.3. Biofunctionalization and applications to FET biosensors

The biofunctionalization can be categorized into covalent and non-covalent approaches. Direct adsorption of bioreceptors on the NWs via vdW and electrostatic forces enables the non-covalent functionalization (**Fig. 6 (b)**). The high IEP of metal oxides, such as ZnO and TiO_2, enables the direct biofunctionalization of bioreceptors (enzymes, antibodies, DNA probes, etc.) with low IEP via electrostatic interaction. Many metal oxides have been functionalized with biomaterials via physical adsorption (Gao et al., 2012; Mun et al., 2010; J. Wang et al., 2015). On the other hand, the surfaces of metal oxide NWs are naturally advantageous in providing oxygenated moieties for biofunctionalizations (**Fig. 6 (c)**). One strategy applied to immobilize bioreceptors on In_2O_3 is to use a self-assembled monolayer (SAM) of hydroquinone (HQ) and its derivatives to provide the peptide ligand for cell adhesion (Eckermann et al., 2010; Yeo et al., 2003). It was further promoted to a selective method of functionalizing DNA probes on In_2O_3 NWs by using 4-(1,4-dihydroxybenzene)butyl phosphonic acid (HQ-PA) to form SAM on In_2O_3 NWs. The oxidized HQ-PA (Q-PA) conjugates with functional groups, such as thiol, amine, azides, and cyclopentadienes (Curreli et al., 2008, 2005; Lee and Kim, 2012). Cheung et al. functionalized the thiolated ssDNA on In_2O_3 FETs using m-maleimidobenzoyl-NHS as the thiol-amine linker (Cheung et al., 2020). Besides, non-covalent linker is also widely used for immobilizing bioreceptors. Organosilane, such as APTES, can attach to the surface with -OH groups, and conjugate to biomolecules with active amine groups (Li and Liu, 2017; Williams et al., 2014). **Table 4** summarizes recently reported FET biosensors by researchers from North America using these nanomaterials with improved sensing capabilities.

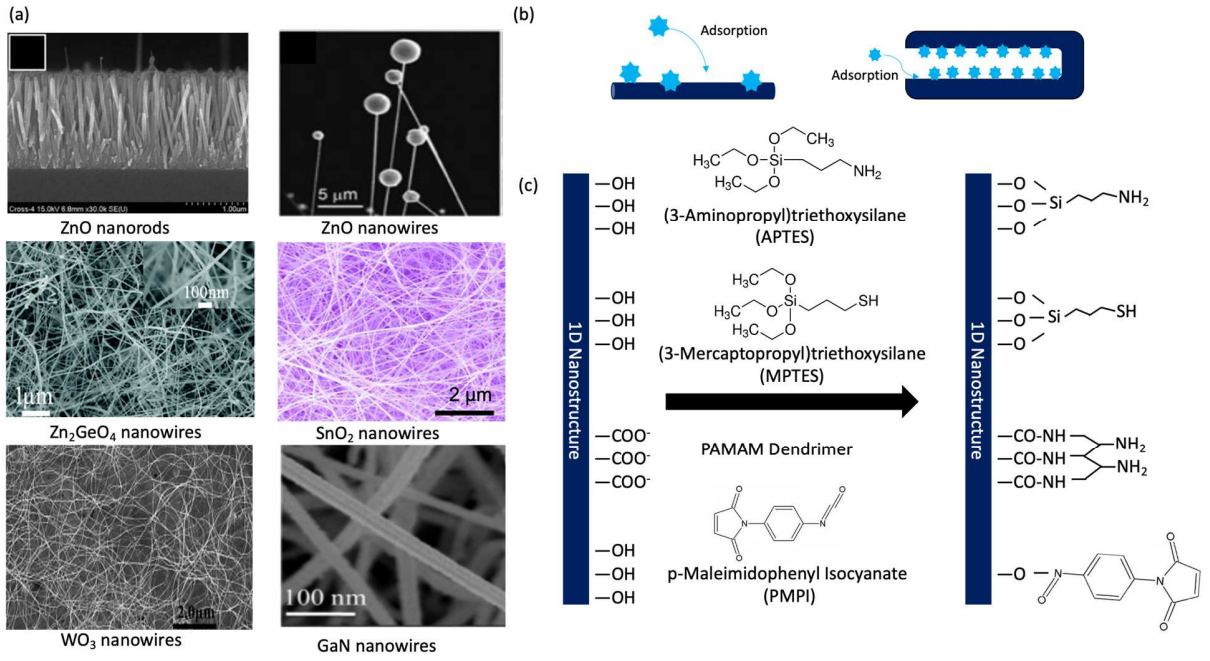

Fig. 6. Structures of other 1D nanomaterials and biofunctionalization strategies. (a) SEM images of some common 1D nanostructures for FET biosensors. SEM of the ZnO nanorods is reprinted from *Biosensors and Bioelectronics 45 (2013): 281-286*. (Ahmad et al., 2013) Copyright (2013), with permission from Elsevier. SEM of the ZnO nanowires is reprinted from (Pan et al., 2005) *Angewandte Chemie International Edition 44.2: 274-278 (2005)*. Copyright Wiley-VCH Verlag GmbH & Co. KGaA. Reproduced with permission." SEM of the Zn_2GeO_4 nanowires is reprinted from (Han et al., 2019). SEM of the SnO_2 nanowires is reprinted with permission from (Dattoli et al., 2007). Copyright (2007) American Chemical Society. SEM of the WO_3 nanowires is reprinted from *Materials Science and Engineering: C 53 (2015): 43-49*. (Liu et al., 2015) Copyright (2015), with permission from Elsevier. SEM of GaN nanowires is reprinted from *Biosensors and Bioelectronics 44 (2013): 164-170*. (Sahoo et al., 2013). Copyright (2013), with permission from Elsevier. (b) Physical adsorption of bioreceptors to the 1D nanomaterials. (c) Some common surface modification strategies for biofunctionalization.

Table 4. Summary of FET biosensors based on metal oxide NWs and other 1D nanomaterials by North American institutes since 2010.

1D nanomaterial	**Bioreceptor**	**Analyte**	**LOD**	**Linker**	**Ref.**
GaN NWs	PEG-biotin	Streptavidin	-	-	(Guo et al., 2010)
GaN NWs	Biotin	Streptavidin	-	-	(Williams et al., 2014)
In_2O_3 NWs	Antibody	CA-125 and IGF-II	0.5 pM (CA-125) and 8 ng/mL (IGF-II)	11-Mercaptounde canoic acid	(Chang et al., 2011)

In_2O_3 NWs	Antibodies	cTnI, CK-MB, and BNP	1 ng/mL (cTnI), 0.1 ng/mL (CK-MB), and 10 pg/mL (BNP)	Phosphonic acid	(Liu et al., 2016)
In_2O_3 nanoribbons	Glucose/chitosan/ SWCNT hybrid	Glucose	10 nM	-	(Liu et al., 2018)

4. 2D nanomaterials-based FET biosensors: structure and properties, synthesis, biofunctionalization and featured applications.

4.1. Graphene, graphene oxide and reduced graphene oxide

4.1.1. Structure and properties

Graphene is a single layer of covalently bonded carbon atoms in a honeycomb lattice. Each carbon atom is bonded to three other carbons with a sp^2-hybridization. Its bulk hexagonal structure, graphite, is a vdW material with an interlayer distance of 3.35 Å. The layered nature of graphite and the weak interlayer vdW bonding facilitate its mechanical exfoliations into graphene, or chemical exfoliation into GO. The electrical conductivity in graphene can be discussed in different mechanisms, but the most predominant mechanism is the delocalization (resonance) of π-bonds in the conjugated systems of sp^2 carbons of graphene, with a constant bonding/nonbonding action (Shu and Chou, 2012). Differently, GO is decorated with oxygen functionalities in the basal plane and on edges, which in-turn disrupts the conjugation by introducing a large portion of sp^3 C-C hybridizations. By removal of oxygen atoms from the GO sheets, or in other words, by reducing it into rGO, the insulative GO structure is reversed to semi-metallic graphene (Eda et al., 2009). **Fig. 7** shows schematic structures of graphite, graphene, GO, and rGO.

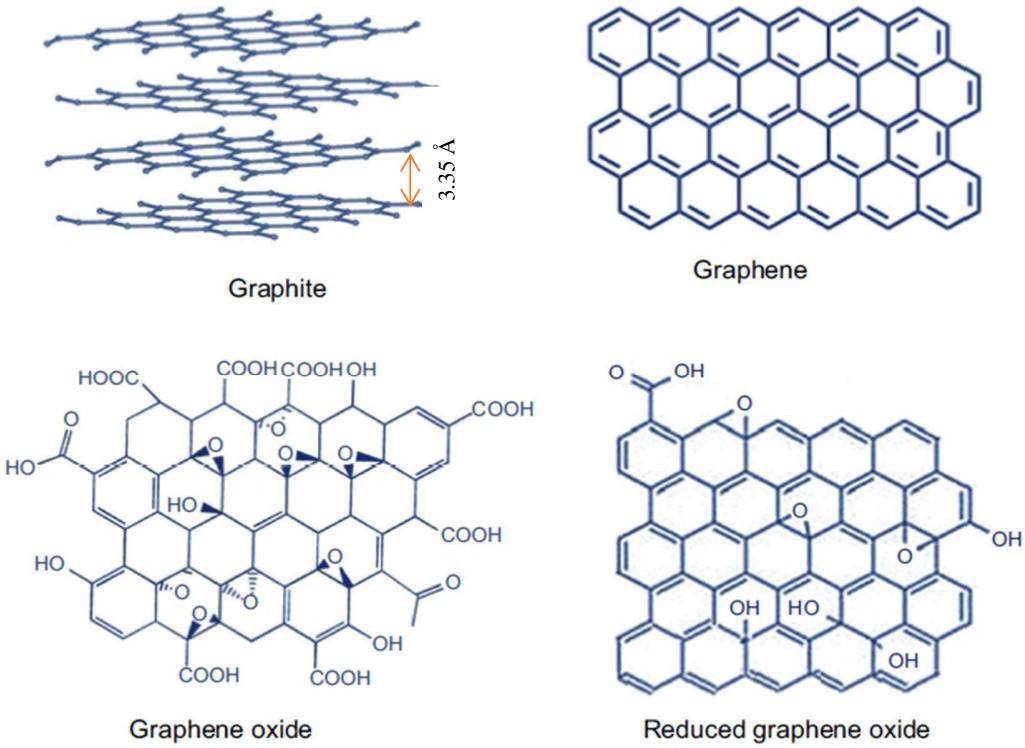

Fig. 7. Schematic structures of graphite, showing its interlayer distance; graphene, with its conjugation of double and single bonds; GO, with the defected structure due to oxygen functionalities; rGO, with less defects due to the healing reduction process. Reprinted from (Bai et al., 2019).

Graphene has fascinating electrical properties of extremely high carrier mobility of (200,000 $cm^2\ V^{-1}\ s^{-1}$), and room temperature resistivity of 10^{-6} Ω m that is thickness-dependent (Bolotin et al., 2008). In addition, graphene possess a high theoretical specific surface area of 2630 $m^2.g^{-1}$ that is twice of SWCNTs (Bonaccorso et al., 2015). Due to all these interesting electronic properties, as well as its high sensitivity to electronic perturbations from analyte molecules adsorption, graphene has been widely used in FET biosensors. The good sensitivity of graphene is attributed mainly to its high surface area and high carrier mobility (Mao et al., 2017; Meng et al., 2019). However, the lack of intrinsic band gap and low current on/off ratio strongly affect its sensitivity and limit its FET applications (Zhang and Lieber, 2016). On the other hand, GO is another form of graphene that is easy to scale up, economic, and contain desirable oxygen functionalities for further surface modifications (Boukhvalov and Katsnelson, 2009; Pei and Cheng, 2012; Zhu et al., 2010). In addition, GO is highly dispersible in water and forms stable suspensions for printed electronics (Le et al., 2011; J. Lee et al., 2019; G. Wang et al., 2015). GO's reduction can be optimized to prepare graphene with tunable band gaps (Acik and Chabal, 2013).

4.1.2. Synthesis of graphene, rGO, and crumpled graphene/rGO

Graphene is a layered material that can be prepared by top-down or bottom-up methods. Top-down approach relies on exfoliation of graphite using micromechanical (e.g. scotch tape) or liquid phase exfoliations (LPE). Micromechanical exfoliation was first introduced by Novoselov and Geim where they peeled off graphene from graphite using a scotch tape (Novoselov et al., 2004), and it is the best method to prepare defect-free graphene for fundamental studies or lab scale. LPE of graphite into graphene is a very promising exfoliation method that overcomes the limitations of micromechanical exfoliation as it is economic, easy to scale up, and simple (Amiri et al., 2018). Nevertheless, it has its downsides, such as difficulty to remove the surfactants and solvents due to their high boiling point and the possibility of introducing edge and basal plane defects owing to prolonged high power sonication (Amiri et al., 2018; Ramnani et al., 2016). Electrochemical methods are also applied to exfoliate graphite into graphene nanosheets (H. Lee et al., 2020). As a bottom-up technique, CVD is used to synthesize graphene by deposition of hydrocarbons vapor on a substrate (e.g. Cu, Ni, or SiC) at elevated temperatures (> 600 ^{o}C), under inert/reducing gas conditions (Ar/H_2) (Zhang et al., 2013). On the other hand, GO can be synthesized by the chemical exfoliation (e.g. Hummer's method and its modified/improved versions) of graphite using strong oxidizing agent ($KMnO_4$) in presence of a highly acidic medium (H_2SO_4 and H_3PO_4) (Marcano et al., 2010). To restore the electronic properties of pristine graphene, GO is reduced to rGO using thermal, chemical, electrochemical methods, where all/most of the oxygen functionalities are removed (Bennett et al., 2016; Kumar et al., 2016; Stankovich et al., 2007). Crumpled rGO (C-rGO) can be prepared by rapid evaporation of GO aerosol droplets, forming submicrometric rGO crumples (Deng and Berry, 2016; Gao et al., 2018; Luo et al., 2011). Rapid drying of GO has achieved a nanometer crumpling in rGO (Ma et al., 2012). Crumpling happens under rapid heating and solvent evaporation under isotropic compression and expansion of GO sheets. For controlled crumpled/uncrumpling of graphene, the large area graphene is transferred to a pre-stretched elastomer surface, where the biaxial relaxation of the elastomer forms crumpled graphene, and stretching it again uncrumples graphene (Zang et al., 2013). Other elastomers that shrink by heating, such as polystyrene, were used to prepare C-graphene, where graphene/polystyrene were heated to 110 ^{o}C for 2 h to shrink the polymer and crumple graphene (Hwang et al., 2020). **Fig. 9** shows a schematic of the fabrication of flat and crumpled graphene FET biosensors for DNA/RNA detection.

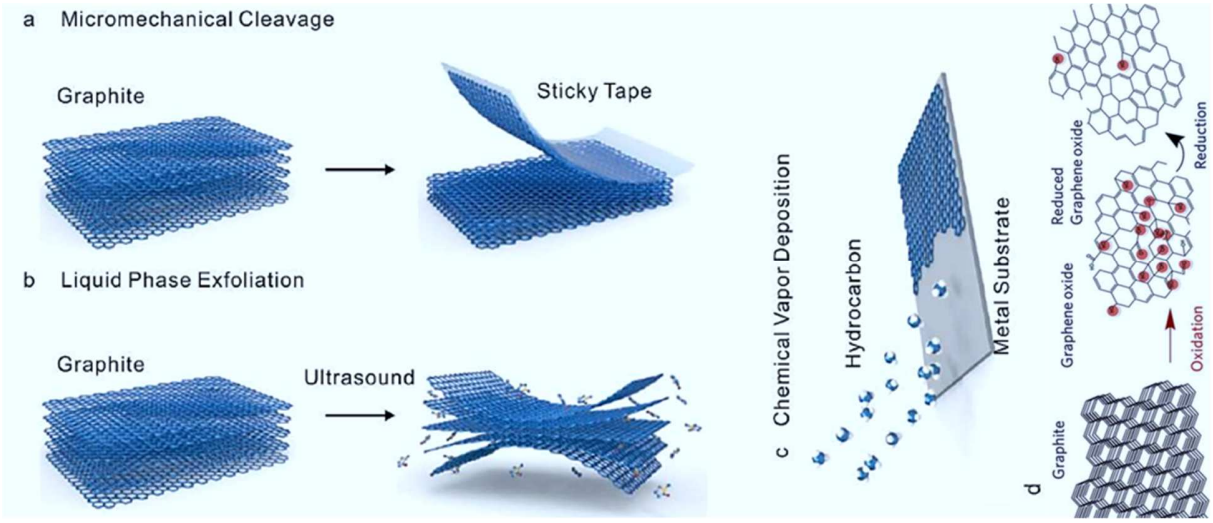

Fig. 8. Schematic diagrams of the different methods used in synthesis of (a-c) graphene, adapted from (J.-H. Lee et al., 2019), and (d) rGO nanosheets, adapted from (Khairir et al., 2015).

4.1.3. Biofunctionalizations and applications to FET biosensors

Graphene is the main building block of CNTs, and hence they have a similar chemistry. So, the surface functionalization of graphene is very similar to CNTs. Graphene/rGO can be functionalized with bioreceptors using linkers, that bind from one side to graphene, and from the other side to bioreceptors via different functional groups (carboxyl, hydroxyl, aldehyde, amine, thiol, etc.). Linkers can bind to graphene either through covalent bonding by targeting the C=C bonds of graphene using 1,3 dipolar cycloaddition of azomethine ylide, or via non-covalent bonding using π–π stacking of pyrene compounds such as 1-pyrenebutanoic acid N-hydroxysuccinimidyl ester (PBASE) to the basal plane of graphene/rGO nanosheets (Georgakilas et al., 2012; Viswanathan et al., 2015). Then, PBASE reacts readily with bioreceptors. In addition, direct adsorption of bioreceptors to graphene/rGO is another alternative (Hwang et al., 2020; Wang et al., 2011). For GO and partially reduced GO, they contain carboxyl groups that can be directly bonded to the bioreceptor molecules using carbodiimide crosslinking chemistry (Krishnan et al., 2019; Zaid et al., 2017).

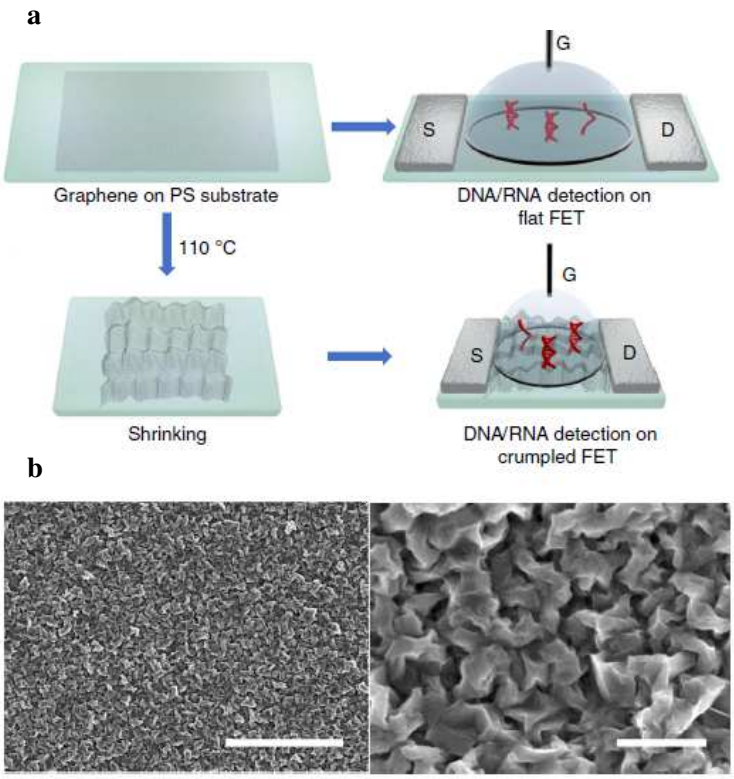

Fig. 9. (a) A schematic of the flat and crumpled graphene on polystyrene (PS) for detection of DNA/RNA. (b) SEM images of flat (left) and crumpled (right) graphene. The scale bar is 5 μm (left) and 500 nm (right). Adapted from (Hwang et al., 2020).

Graphene materials have been widely used as channel materials in FET biosensors and there is a huge number of graphene- and rGO-FET biosensors introduced by North America that are summarized in **Table 5**. Moreover, deformed graphene (wrinkled and crumpled) has started attracting attention (Gilbonio et al., 2020; Hwang et al., 2020). For instance, crumpled graphene has been recently reported to enable much higher sensitivity to biomolecules (e.g. miRNA) compared to flat graphene (Hwang et al., 2020). The higher sensitivity was attributed to the increase in λ_D that reduced charge screening, as well as opening band gap in bending sites of graphene and the generation of electrical hot spots.

Table 5. Summary of graphene materials-based FET biosensors developed by North America in 2010-2020.

2D nanomaterial	Bioreceptor	Analyte	LOD	Linker	Ref.
Graphene	Cytochrome C	H_2O_2	100 fM	1,5-diaminonaphthanlene-glutaraldehyde	(S. H. Lee et al., 2020)
Graphene	Antibiotics	Gram-negative and -positive bacteria	1–9 CFU/mL	PDA and PANHS	(Kim et al., 2020)
Graphene	Aptamer	human immunoglobulin E (IgE)	47 pM	PBASE	(Wang et al., 2018)
Graphene	Pyrene-tagged Aptamer	*E. coli*	10^2 CFU/mL	--	(Wu et al., 2017)
Al_2O_3/rGO	DNA	Hg^{2+}	1 nM	Self-assembly of DNA on AuNPs	(Chang et al., 2015)
rGO	Aptamer RNA	Antibiotic (tobramycin)	0.3 nM	Self-assembly of aptamer on AuNPs	(Chen et al., 2019)
Al_2O_3/rGO	Anti-E. coli antibody	*E. coli*	Single cell	Self-assembly on AuNPs	(Thakur et al., 2018)
Al_2O_3/rGO	Anti-Ebola antibody	*Ebola glycoprotein*	1 ng/mL	Self-assembly on AuNPs	(Y. Chen et al., 2017b)
Graphene	DNA	miRNA let-7b	2 pM	PBASE	(Hwang et al., 2020)
Crumpled graphene	DNA	miRNA let-7b	600 zM	PBASE	(Hwang et al., 2020)

PDA is bis(2-aminoethylene)perylene-3,4,9,10-tetracarboxyldiimide. PANHS and PBASE are different names for the same compound and it is 1-pyrenebutyric acid N-hydroxysuccinimide ester.

4.2. Transition metal dichalcogenides

4.2.1. Structure and properties

TMDCs are another family of 2D layered materials with the general structure of MX_2 (X-M-X), where M is a transition metal (Ti, Zr, Hf; V, Nb, Ta; Ct, Mo, or W), from groups IV, V, and VI, that is sandwiched between two chalcogen (X) atoms (S, Se, or Te). Analogous to graphene, bulk TMDCs form weak vdW bonding between layers and strong covalent or ionic bonds in the same layer, i.e. between M and X, which makes it easy to exfoliate them. Each transition metal atom is surrounded by six chalcogen atoms in an octahedral, forming *1T* phase, or triangular prism coordination, forming *2H* phase (Lv et al., 2015). The type of coordination depends on the nature of bonding between transition metal and chalcogen; group IV transition elements form strong ionic bonds, which result in repulsive Coulomb forces between layers, and hence octahedral coordination is more favoured. Contrarily, group VI transition elements form covalent compounds, and stabilize well in trigonal prismatic coordination (Wilson and Yoffe, 1969; Zong et al., 2008). Due to their moderate ionicity, group V elements can be found in both octahedral and trigonal prismatic coordination (Y. J. Zhang et al., 2015). **Fig. 10** shows the two coordination types (octahedron and trigonal prism) and the two most common phases of TMDCs (*2H* and *1T*). Due to their intriguing optical and electronic properties, TMDCs have garnered a huge attention for the application in FET biosensors. Based on their phase and the number of d-electrons, TMDCs vary between semi-metallic, semiconductors, insulator, or superconductors. As most TMDCs are semiconductor (e.g. MoS_2, $MoSe_2$, WS_2, WSe_2), compared to the semi-metallic graphene, they are more promising as electronic switches in FET sensors (Kutana et al., 2014; Meng et al., 2019). MoS_2, owing to is very high on/off current ratio ($\approx 10^8$) (Islam et al., 2018; Wu et al., 2013) was the first TMDC to attract attention as a strong material for FET sensors. Semiconductor TMDCs, such as MoS_2 have an indirect band gap in bulk-state, a larger direct band gap and a strong photoluminescence (PL) when they are mono- or few-layers (Z. Li et al., 2015). It is worth mentioning that the band gap and PL emission of TMDCs are tuneable and size- and composition-dependent.

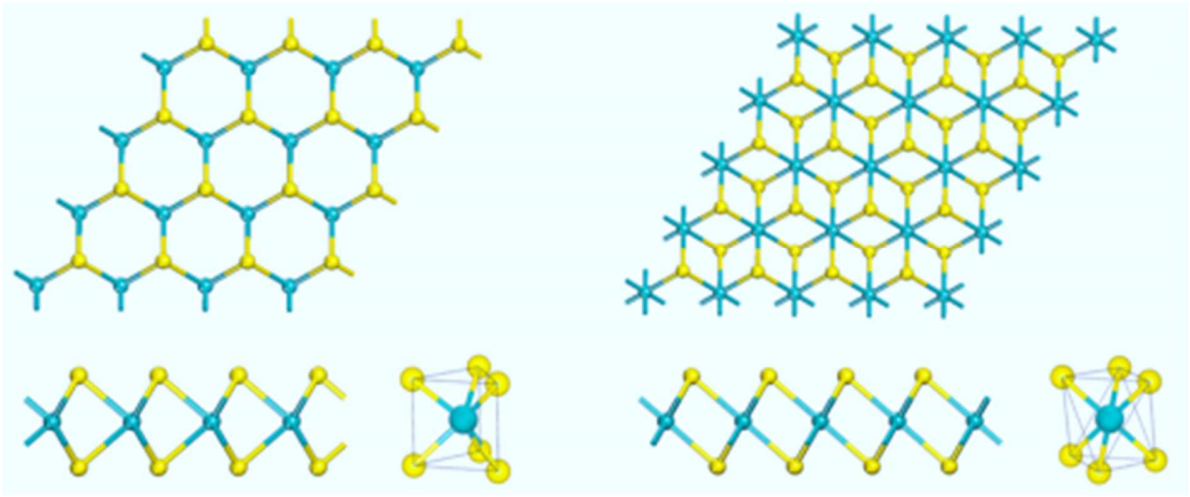

Fig. 10. A schematic representation of the crystallographic structure of MoS_2, showing the 2H (left) and the 1T (right) phases, from top and side views. Reprinted from (Tang and Jiang, 2015).

4.2.2. Synthesis of TMDCs

TMDCs can be synthesized by means of exfoliation of their bulk crystals or from their atoms via vapor phase deposition (Zhang, 2015). Mechanical exfoliation is the first choice for proof-of-concept devices or fundamental research. However, it is not suitable for scaling up and controlling the number of layers is difficult. LFE using chemicals is another approach that is preferred for solution-based or printable electronics. LPE is scalable and easy to process and handle, however, it introduces extrinsic defects to the crystals, altering the intrinsic properties of the synthesized material (Chen et al., 2020). On the other hand, the bottom-up approach utilizes different techniques, but they all rely on the vapor deposition on a substrate. First technique is sulfurization/selenization of pre-deposited transition metals or their oxides on a substrate (e.g. SiO_2/Si or Sapphire), followed by annealing at 500-1000 ^oC with sulfur or selenium vapor. This technique allows for a large area and high throughput synthesis of TMDCs, however, the quality of produced nanosheets is governed by the quality of pre-deposited metal/metal oxide, which is hard to control. Moreover, most of the prepared TMDCs are polycrystalline (Shi et al., 2015). Second technique is CVD, which is the most reported method that can produce high quality, large area, and controlled thickness TMDCs. In addition, alloys of ternary compounds, such as Mo-$Se_{2(1-x)}Te_{2x}$ can be synthesized using this method (Apte et al., 2018). Briefly, vapor of transition metal oxide and chalcogen are carried out to the reaction furnace tube containing a substrate (e.g. SiO_2/Si or Sapphire), using Ar or N_2 as inert carrier mixed with a reducing gas (H_2). The two vapors react at certain temperature and deposit on the substrate surface to complete their crystallization (Zhou et al., 2018).

4.2.3. Biofunctionalizations and applications to FET biosensors

Surface functionalization is a crucial step for the successful building of TMDCs-FET biosensors that can be divided into four main categories: sulfur-vacancy modification, covalent modifications using electrophiles such as diazonium salts, Au-assisted functionalization, and surface coverage with metal oxide. Sulfur-vacancy modification strategy utilizes sulfur vacancies in MoS_2 or WS_2 (Lin et al., 2016) and fill them with organic thiols (R-SH), so that the exogenous sulfur forms a coordination bond with the transition metal at the S-atom vacancy. In addition, R-SH can be functionalized on the basal plane of MoS_2 directly by sonication with the chemically exfoliated sheets, as shown in **Fig. 11 (a)** (Zhou et al., 2014). The organic part of the linker usually

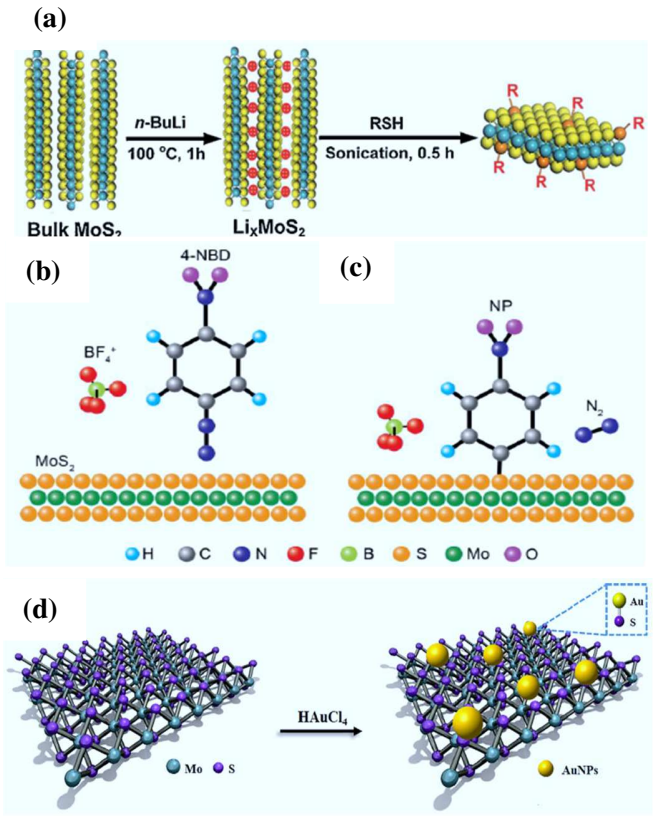

Fig. 11. Surface modifications of TMDCs (MoS_2 was used as an example). (a) Surface modification with organic thiols (R-SH). Adapted from ref. (Zhou et al., 2014) with permission from The Royal Society of Chemistry.. (b) Schematic of the covalent functionalization of MoS_2 using 4-nitrobenzenediazonium tetrafluoroborate (4-NBD) and (c) after functionalization, carbon binds covalently to sulfur (C-S), and N_2 is released. Reprinted with permission from (Li et al., 2019). Copyright 2019 American Chemical Society. (d) Gold decoration on MoS_2 nanosheet. Adapted from (Wu et al., 2018), Copyright 2018, with permission from Elsevier.

contains easy to functionalize groups (e.g. -NH_2 or -COOH). The second method is based on covalent modifications using electrophiles such diazonium salts, which functionalizes not only sheet edges but also basal plane as in **Fig. 11 (b & c)** (Li et al., 2019). In the Au-assisted functionalization, Au nanoparticles are grown on the surface of TMDCs, using different techniques followed by functionalization using thiol-containing linkers, as in **Fig. 11 (d)** (Wu et al., 2018). In metal oxide coverage approach, TMDCs surface is covered by a thin oxide (e.g. Al_2O_3, HfO_2, etc) film, followed by activation with oxygen plasma and then linking to APTES, which can be easily linked to the biorecognition element via its amine groups (Lee et al., 2014). However, this approach deteriorates the sensitivity of the TMDC-FET biosensor by increasing the distance between charged molecules and TMDC surface (Nair and Alam, 2008). There are other possible methods such as physical adsorption of bioreceptors to TMDCs surface, but what we discussed here are the most common methods. It is important to note that most of these surface functionalizations might tune the electronic properties of the corresponding TMDCs (Lin et al., 2016). **Table 6** summarizes some of the TMDC-FET biosensors reported from North America.

4.3. 2D transition metal oxides

4.3.1. Structure and properties

Composed of metal and oxygen, metal oxides (MOs) are among the most diverse solids with a wide range of structures and properties. MOs can be sorted out as layered (e.g. WO_3, Ga_2O_3, MoO_3, and TaO_3) and non-layered (e.g. SnO_2, In_2O_3, ZnO, and CuO) 2D MO (Meng et al., 2019). α-MoO_3 and ZnO_2 are examples of layered and non-layered MOs, respectively. **Fig. 12 (i)** shows the crystal structure of α-MoO_3, which forms an orthorhombic crystal of double layers of edge-sharing MoO_6 octahedra, stacked vertically by vdW weak forces that increases its feasibility for exfoliation. In addition, the Mo-O bonds are a mixture of ionic and covalent bonds (Ding et al., 2012). On the other hand, ZnO exists in three polymorphs: zinc blende, rocksalt, and wurtzite. The thermodynamically favoured hexagonal (wurtzite) lattice of ZnO is more dominant, in which planes of Zn^{2+} and O^{2-} ions are piled alternatively, introducing polarity to the structure that improves its stability. Moreover, the presence of polar and non-polar planes in ZnO triggers strong electrical properties that can be tuned for ZnO-based electrical biosensors (Shanmugam et al., 2017). Another example of non-layered MOs is In_2O_3.As illustrated by **Fig. 12 (ii)**(left), the In-O_x polyhedra link together in corner-sharing, side-sharing, or less commonly by face-sharing polyhedral. Each indium atom is surrounded by six oxygens and two vacancies of missing oxygen [**Fig. 12 (ii)**(right)] (Buchholz et al., 2014).

2D MOs have high chemical stability against air and water due to the termination of their basal planes with oxygen atoms. As mentioned earlier, MOs vary significantly in their structures, and hence they show a huge variation in their electronic properties associated with a wide range of conductivity from metallic to

semiconductor to insulators (Meng et al., 2019). MOs exhibit a wide range of band gaps (2.3–4.9 eV) and relatively high electron mobilities (>10 cm^2 V^{-1} s^{-1}), which allows for high signal-to-noise ratio and high sensitivity in FET biosensors. Additionally, their surfaces can be easily functionalized with bioreceptors due to oxygen termination (H. Chen et al., 2017; Şerban and Enesca, 2020). O^{2-} ions and the ionic nature of M-O bonds are important factors that determine the surface properties of MOs (Mannhart and Schlom, 2010). Additionally, the high concentration of O^{2-} ions in MOs' lattice induces high polarizability that allows 2D MOs to demonstrate large distributions of charges, resulting in a 1-100 nm thick electrostatic screening zone, that in-turn provides MOs with extraordinary local surface and interfacial properties (Mannhart and Schlom, 2010).

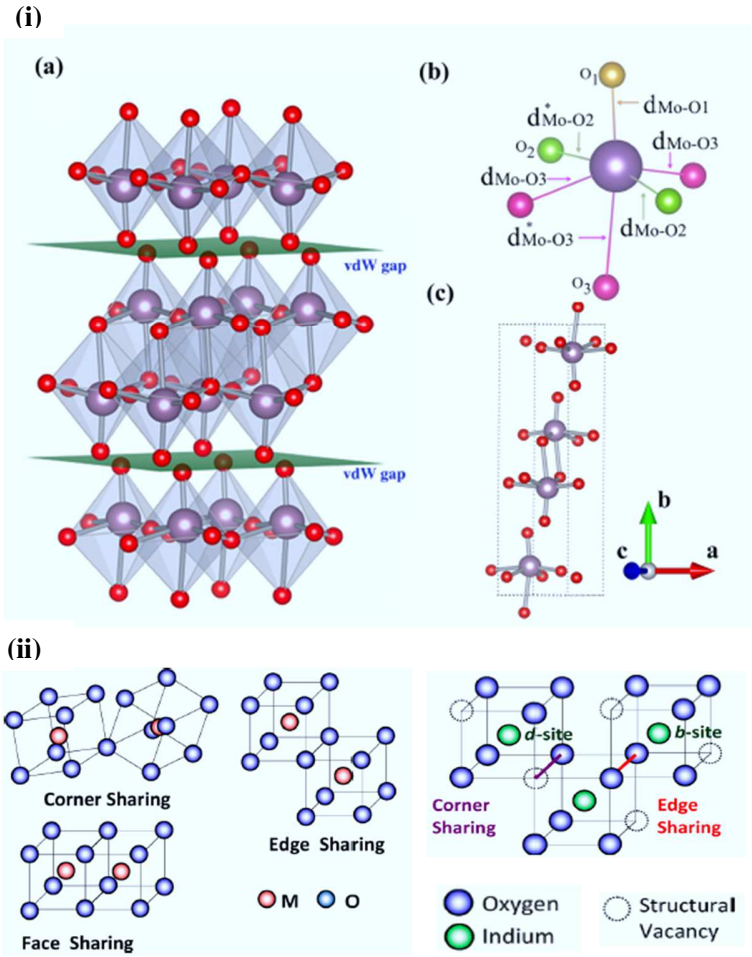

FIG. 12. Crystal structure of α-MoO_3 and ZnO_2. (i) (a) Orthorhombic crystal of d α-MoO_3 showing the double layers of edge-sharing MoO_6 octahedra, where Mo is displayed in purple and O in red, (b) Symmetry of the different oxygen ions

in the MoO_6 octahedron (O1, O2 and O3). (c) The conventional unit cell. "[Fig. 1] Reprinted with permission from (Ding et al., 2012). Copyright 2012 by the American Physical Society." https://journals.aps.org/prb/abstract/10.1103/PhysRevB.85.012104. (ii) (left side) In-O_x polyhedral link together in corner-sharing, side-sharing, or less commonly by face-sharing polyhedral. (ii) (right side) Each indium atom is surrounded by six oxygens and two vacancies of missing oxygen. Reprinted from (Buchholz et al., 2014).

4.3.2. Synthesis of 2D MOs

2D MOs can be synthesized by a variety of methods, including self-assembly, morphological transformations, and salt-template methods (Sun et al., 2014; Xiao et al., 2016). Most of the 2D MOs are synthesized using hydrothermal or solvothermal methods. This can be attributed to the scalability, simplicity, low temperature and cost requirements (J. Li et al., 2015). The synthesis process starts by dissolving nitrates, sulfates, or chlorides of the metals in a suitable solvent (e.g. water or organic solvent), and leaving them to react in a sealed vessel (e.g. Teflon tube) for 3-12 h, in a temperature range of 75-250 ^oC (J. Li et al., 2015; Rim, 2020). In addition, different exfoliation methods have been applied to synthesize 2D layers of MOs for application in FET sensors (Kalantar-zadeh et al., 2010). Another synthesis method of 2D MOs thin films is by spin coating of metal oxide precursor solution (e.g. indium nitrate hydrate) on a substrate and then baking it at 100 ^oC, followed by annealing at 300 ^oC for 3 h (Rim et al., 2015).

4.3.3. Biofunctionalizations and applications to FET biosensors

There are different functionalization techniques that can be applied for surface modification of 2D MOs with bioreceptors, as discussed in 1D metal oxides, section 3.4.3. Covalent functionalization by utilizing the oxygen functionalities on metal oxides surfaces with silanes containing amine (such as APTES) or mercapto-moiety is among the simplest methods (Rim et al., 2015). Non-covalent functionalization through physical adsorption of bioreceptors on metal oxide surface is another alternative. Among the family of 2D MOs, In_2O_3 has shown significant success as a semiconductor sensing material in FET biosensors, as summarized in **Table 6**. The area of 2D metal oxides and their FET-based biosensors is still relatively unexplored and the contribution from North America in this area is still humble.

4.4. Black phosphorus/phosphorene

4.4.1. Structure and properties

BP is another important and relatively new member in the family of layered vdW materials, and its monolayer is known as phosphorene. BP is the most stable phosphorus allotrope, and it forms an orthorhombic crystal structure at ambient temperature and pressure. Like graphene, each phosphorus atom is bonded to three other phosphorus atoms, in a six-membered ring. However, the hybridization of phosphorene is sp^3 and not sp^2 as in graphene. The interlayer separation between BP sheets is 5.239 Å. As shown in **Fig.**

13 (a & b), BP shows out-of-plane and in-plane electronic anisotropy, the former can be attributed to the weak vdW forces between layers compared to the strong covalent bonds in the same layer. The latter is assigned to the out-of-plane distortion in the same layer forming a puckered structure along the armchair direction and a ridge structure along the zigzag (Liu et al., 2017).

Due to the electronic anisotropy of BP, the measured conductivity and carrier mobility were higher in the armchair direction than in the zigzag direction and much higher than in the vertical direction (Xia et al., 2014). BP has a thickness-dependent direct band gap, that varies from 0.3 eV in bulk to 2.0 eV in monolayer (phosphorene). In addition, BP exhibits a high carrier mobility of up to 1000 cm^2 V^{-1} $s^{-1}$and current on/off ratio of 10^5 (obtained for a 10 nm thick sample) (Li et al., 2014; Xia et al., 2014). As a limitation of its applications, BP is highly reactive to air oxygen and humidity due to the presence of lone pair of electrons on each phosphorus atom, which results in an instability in their devices and causes a huge device-to-device variation. Moreover, the anisotropic electrical conductivity results in a device-to-device variation as well (Akhtar et al., 2017).

4.4.2. Synthesis of BP

Few-layered BP and phosphorene can be prepared using different top-down (exfoliation) techniques or through thermal transformation of its allotropes (red phosphorus) (Akhtar et al., 2017). Liquid phase exfoliation of BP, after grinding in mortar and pestle, was successful by low power bath sonication in a sealed tube containing anhydrous deoxygenated organic solvent (isopropyl alcohol, IPA) for 16 h (Woomer et al., 2015). The BP suspension in isopropyl alcohol changed color from black to grey and then to yellow, as the degree of exfoliation progressed (**Fig. 13 (c)**). Sresht et al. conducted an interesting computational work on studying the effect of solvent on liquid exfoliation of BP (Sresht et al., 2015). They studied five solvents: IPA, dimethyl sulfoxide (DMSO), dimethylformamide (DMF), N-methyl-2-pyrrolidone (NMP), and N-cyclohexyl-2-pyrrolidone (NCP). NMP and DMF were proven to be the most efficient among the five, due to their better ability to penetrate between BP layers. Electrochemical exfoliation is another important synthesis route, however, contributions from North America in this area is still limited. A majority of the work in this area is coming from Singapore, such as work of (Li et al., 2018). Baboukani et al. exfoliated BP and deposited it on electrode surface by applying 30 V (DC) in an aqueous solution containing bulk BP (**Fig. 13 (d)**) (Baboukani et al., 2019). For the bottom-up (epitaxial) growth, there was a successful work introduced on CVD synthesis of bulk BP from red phosphorus. However, there is no successful CVD synthesis of phosphorene to-date, to the best of authors' knowledge. This may be attributed to the high chemical reactivity of phosphorene to oxygen (Kou et al., 2015).

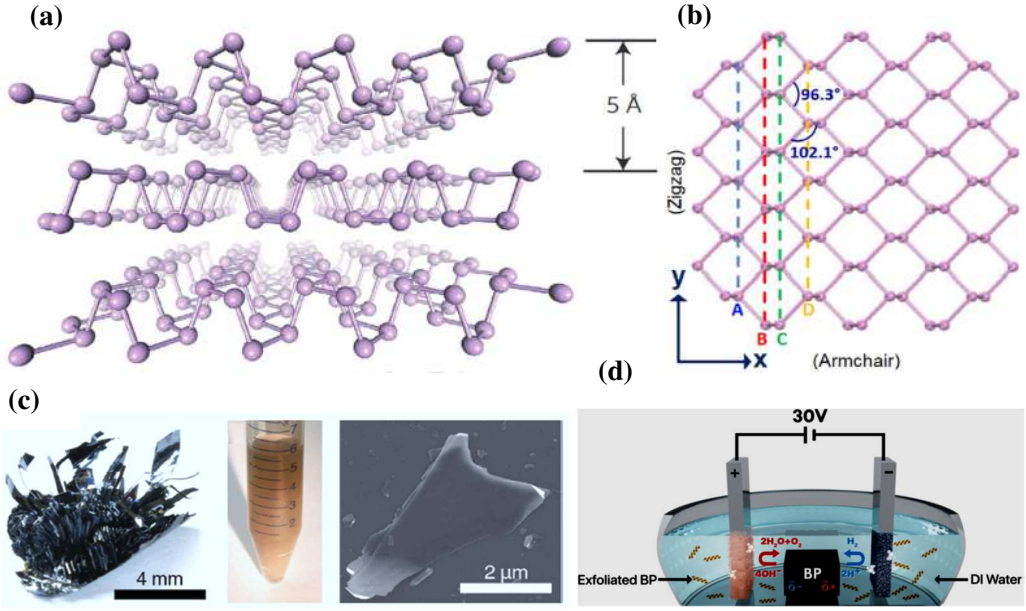

Fig. 13. (a and b) A schematic diagram of the bulk structure of BP and top view of a single layer of BP with armchair and zigzag directions. Adapted from (Mu et al., 2019), Copyright 2019, with permission from Elsevier. (c) photographs of BP, suspension of exfoliated phosphorus in isopropanol, and an SEM image of the exfoliated structure. Adapted with permission from (Kou et al., 2015) Copyright 2015 American Chemical Society. (d) Electrochemical cell for the exfoliation of BP. Reprinted from ref. (Baboukani et al., 2019) with permission from The Royal Society of Chemistry.

4.4.3. Biofunctionalizations and applications to FET biosensors

Despite its high carrier mobility, conductivity, and current on/off ratio, BP applications in FET biosensors is still relatively unexplored and the contribution from North American research in this area is still modest, as shown in **Table 6**. This might be assigned for its aforementioned instability, and device variations, as well as the more critical requirements of biosensors of incubation in buffers for longer times. For a higher stability of its biosensors, BP is usually coated with a polymer or passivated with a thin metal oxide layer. Biofunctionalizations can be by direct binding of bioreceptor to the polymer coating layer (e.g. poly-L-lysine) (Kim et al., 2017), or by depositing AuNPs on the coating metal oxide layer (e.g. AuNPs/Al_2O_3), followed by bioreceptor functionalization (Y. Chen et al., 2017a).

Table 6. Summary of non-carbon 2D materials (TMDCs, 2D MOs, and BP)-FET biosensors developed in North America in the last decade.

2D nanomaterial	Bioreceptor	Analyte	LOD	Linker	Ref.
MoS_2	Anti-PSA antibody	PSA	1 pg/mL	Linker-free, adsorption	(Lee et al., 2014)
HfO_2/MoS_2	Biotin	Streptavidin	100 fM	APTES	(Sarkar et al., 2014)
Al_2O_3/MoS_2	Anti-PSA antibody	PSA	100 fg/mL	APTES	(Park et al., 2017)
In_2O_3	Glucose oxidase	D-glucose	100 µM	APTES	(Rim et al., 2015)
In_2O_3	DNA aptamer	glucose, serotonin, dopamine	10 pM, 30 nM, 150 nM	Silane (APTMS & PTMS)	(Nakatsuka et al., 2018)
In_2O_3	Boronic acid	Glucose	< 7 fM	APTES & glutaraldehyde	(H. Chen et al., 2017)
In_2O_3	ssDNA	DNA, RNA	--	Silane (APTES & APTMS)	(Cheung et al., 2020)
BP	Anti-AFP antibody	alpha-fetoprotein (AFP)	0.1 ppb	Poly-L-Lysine	(Kim et al., 2017)
Al_2O_3/BP	Anti-HIgG antibody	HIgG	10 ng/mL	AuNPs-Cysteamine-glutaraldehyde	(Y. Chen et al., 2017a)

5. Summary, challenges, and future perspectives

In summary, the tremendous progress in the field of 1D/2D materials has helped develop FET biosensors for label-free sensing with higher sensitivity and lower limits of detection, down to a single molecule. The enhancement in FET sensor sensitivity can be attributed to the unique structural, physicochemical, and electronic properties of 1D and 2D materials (e.g. ultrahigh surface areas, high on/off ratios, and high carrier mobilities). FET biosensors exhibit high sensitivity to biomolecule detection; however, the sensing capability was often hindered by not only the ionic screening effect in highly ionic physiological samples, but also the

various interfering biological species. Solutions to these limitations range from "desalting" the sensor surface by diluting the local sensing matrix and employing smaller probes, such as antibody fragments, nanobodies, and aptamers, to increase/improve the sensitivity; and blocking the nonspecific binding with Tween-20, ethanolamine, bovine serum albumin, and 6-mercaptohexanol to improve the selectivity/specificity. Additional strategies of signal enhancements have been reported (Zafar et al., 2018) and reviewed (Vu and Chen, 2019). Another critical challenge is the repeatability and reliability of the FET-based biosensors. Due to the nature of FET biosensing principle, the sensor responses are dependent on several parameters, such as the quality of nanomaterial, the consistency of the fabrication of nanoscale biosensors, the conjugation efficiency of the bioreceptors, and the susceptibility of the ionic sample matrices. Therefore, the study of the stability, repeatability and reproducibility have always been the inescapable part of the development of the FET biosensors.

1D nanomaterials with the nanometer-scale diameters show high aspect ratios, and have 1D quantum confinement, hence the charge carriers do not shunt around the interaction zone, leading to significantly larger depletion/accumulation of the charge carriers deep into the entire 1D semiconductor, compared to the planar sensors (Chartuprayoon et al., 2015). SiNWs, SWCNTs, and CPNWs have been materials of choice in FET biosensors, due to their high current switching characteristics (on/off ratio), high surface-to-volume ratio and similarity of λ_D to the sensing material's diameter (Tran et al., 2020). Furthermore, CNTs have fascinating physicochemical properties of tuneable conductivity, from insulative to exceptionally conductive, high thermal and chemical stability, and the ease to immobilize bioreceptors, as well as their high surface area and high current on/off ratio. However, there are some limitations in the application of these 1D nanomaterials to FET biosensors, such as inconsistent contacts with S-D electrodes, the difficulty to get pure conductive or semiconductive CNTs instead of getting a mixture of semiconductive/conductive CNTs that impacts their electronic properties, as well as their low carrier mobility, and chemical instability of SiNWs that requires surface passivation.

For 2D nanomaterials, their large surface area (all atoms react with the analyte, leaving no bulk non-reacting atoms), high carrier mobility, high mechanical strength, and flexibility make them ideal candidates for FET biosensors. Furthermore, 2D nanosheets are large in lateral size, which provides more consistent contacts with S-D electrodes and thus reduces the inter- and intra-device variations. Due to its high sensitivity to electronic perturbations from analyte molecule adsorption, graphene has been widely used in FET biosensors. The good sensitivity of graphene is attributed mainly to its high surface-to-volume ratio and high carrier mobility. However, the lack of intrinsic band gap and low current on/off ratio in graphene strongly affect its sensitivity and limit its FET applications (Zhang and Lieber, 2016). On the other hand, GO is another form of graphene that is easy to scale up, economic, and contain desirable oxygen functionalities for further surface

modifications. In addition, GO is highly dispersible in water and forms stable suspension for printed electronics or other applications that require graphene thin films. A reduction process to form rGO is crucial, as GO has a very poor conductivity. However, it is challenging to produce defect-free or even slightly defected rGO. Crumpled graphene has proven to incredibly enhance the sensitivity of graphene-FET biosensors, achieving an attomolar limit of detection of biomolecules, compared to flat graphene. This enhancement was attributed to offering a larger λ_D and formation of electrical hot spots. Semiconducting TMDCs exhibited interesting electronic properties in the nanoscale, such as high current switch ratio, 10^3-10^8, as well as high chemical stability that enabled high sensitivity and stability of the corresponding TMDC-FET biosensors. Nevertheless, their epitaxial (e.g. CVD) growth is not well controlled, causing inter- and intra-device variations, due to the variation in grain sizes, defects, and film continuity. More room is still there for investigating epitaxial growth of the new TMDCs and their alloys. Phosphorene is another strong candidate 2D material for FET biosensors, due to its higher carrier mobility and device current, as well as its high $I_{on/off}$ ratio. Yet, its susceptibility to rapid degradation in air is a major challenge against its applications in FET biosensors. Furthermore, phosphorene's in-plane anisotropy causes more variations from a device to another, especially with the difficulty to determine the exact orientation of the material. To overcome this limitation, a thin film coating (e.g. metal oxide or polymer) is used to help protect it from air, however, this reduces the device sensitivity (Kim et al., 2017; Y. Chen et al., 2017a). So, more effort is still needed to solve the chemical instability problem of phosphorene. 2D MOs have high chemical stability against air and water due to the termination of their basal plane with oxygen atoms. Additionally, the high concentration of O^{2-} ions in MOs' lattice induces high polarizability that allows 2D MOs to demonstrate large distributions of charges, resulting in a 1-100 nm thick electrostatic screening zone, that in-turn provides MOs with extraordinary local surface and interfacial properties. In_2O_3 exhibited a huge potential for FET biosensors.

It is very clear that these new 2D materials (TMDCs, phosphorene, and 2D metal oxides) have shown a great success on lab scale, however they are still far from clinical applications. In addition, the number of studies of these 2D materials-FET biosensors is still very modest. Part of the problem is that these materials are relatively new to the scientific community. More important to consider is the reproducibility problem originating from the lack of robust synthesis protocols and in some cases the chemical instability of the materials (e.g. phosphorene). In addition, biosensors require incubation of the device with materials in solution for hours, which creates a huge material-device stability challenge. CNTs, SiNWs, CPNWs, and graphene materials have had more chances to be implemented in FET biosensors, understand their limitations, and finding some practical solutions, as they were found much earlier than the aforementioned new nanomaterials. TMDCs, phosphorene, metal oxides and other 1D/2D materials need more time and effort to mature and be applied in clinical applications. Creating a library of the new 1D/2D materials, with

tabulated physicochemical and electronic properties would be very useful for researchers/developers to find the suitable material for FET biosensors. **Table 7** summarizes advantages, disadvantages, and possible solutions to disadvantages of the 1D and 2D materials used in FET biosensors.

Table 7. Summary of advantages, disadvantages, and solutions for the disadvantages of 1D and 2D nanomaterials with respect to their FET biosensors.

Nanomaterials	Advantages	Disadvantages	Possible solutions
Carbon nanotubes	- High aspect ratio, electrical conductivity, elastic modulus, carrier mobility, and $I_{on/off}$ ratio. - Versatile functional groups for bioconjugation.	- Impurities in CNT synthesis. - Bundle formation. - Mixed metallic and semiconductor tubes.	- Purification to remove impurities. - Avoid bundle formation by using chemical oxidization, non-covalent modification, surfactant, and sonication.
Conducting polymer nanowires	- High aspect ratio, surface area, electrical conductivity, and tunable solubility. - Short transport path of analyte to wire surface. - Direct functional groups for bioconjugation.	Templated synthesis requires harsh chemicals, after-synthesis alignment, and multiple functionalization steps.	Use template-free and one-step methods, such as electrodeposition, and dopamine-assisted synthesis.
Silicon nanowires	- High surface area, charge mobility, $I_{on/off}$ ratio and low leakage currents. - Tunable bandgap and other electronic properties.	Limited functional groups directly available for bioconjugation.	Use silanization to anchor bioreceptors; introduce amine groups by UV-treated alkyne or alkene.
Other 1D nanomaterials	High surface area, charge carrier mobility, $I_{on/off}$ ratio, transparency, and flexibility.	Reduction in size is limited.	Use bottom-up synthesis
Graphene, graphene oxide, and reduced graphene oxide	- For all 2D materials, they have large surface area (all atoms react with the analyte, leaving no bulk non-reacting atoms), and 2D nanosheets are large in lateral size, which provides more consistent contacts with S-D electrodes and thus reduces the inter- and intra-device variations. - High mechanical strength, and flexibility. - Very high electrical conductivity and carrier mobility.	The lack of intrinsic band gap and low $I_{on/off}$ ratio in graphene strongly affect its sensitivity.	Doping should help introduce a tunable band gap.

	- GO is highly dispersible in water and forms stable suspension for printed electronics or other applications that require graphene thin films		
Transition metal di-chalcogenides	- High current switch ratio, 10^3-10^8. - High chemical stability.	Their epitaxial (e.g., CVD) growth is not well controlled, causing inter- and intra-device variations.	More room is still there for investigating epitaxial growth of the new TMDCs and their alloys.
Black phosphorous/phosphorene	- High carrier mobility and electrical current, as well as its high $I_{on/off}$ ratio	- Susceptibility to rapid degradation in air. - In-plane anisotropy causes inter-device variations.	- Thin film coating (e.g., metal oxide or polymer) is used to help protect it from air. - More work is still needed to solve the inter-device variations.
2D transition metal oxides	- High chemical stability against air and water. - Eextraordinary local surface and interfacial properties. In_2O_3 exhibited a huge potential for FET biosensors.	None reported.	None reported.

Author Contributions: M.S., Y.S. and A.M. wrote and edited the manuscript. All authors have read and agreed to the published version of the manuscript.

Funding: This work was supported by grants from the National Science Foundation (1842718), Department of Energy (under award number FE0030456), National Institute of Justice (2019-NE-BX-006) and UC Riverside and Korea Institute of Materials Science (Research Program (POC2930)) through UC-KIMS Center for Innovation Materials for Energy and Environment. A.M. recognizes the W. Ruel Johnson Chair in Environmental Engineering.

Conflicts of Interest: The authors declare no conflict of interest

References

Acik, M., Chabal, Y.J., 2013. J. Mater. Sci. Res. 2.1, 101.

Ahmad, R., Tripathy, N., Hahn, Y.-B., 2013. Biosens. Bioelectron. 45, 281–286.

Ahn, J., Choi, S., Han, J., Park, T.J., Lee, S.Y., Choi, Y., 2011. IEEE Trans. Nanotechnol. 10, 1405–1411.

Akhtar, M., Anderson, G., Zhao, R., Alruqi, A., Mroczkowska, J.E., Sumanasekera, G., Jasinski, J.B., 2017. npj 2D Mater. App. l.1, 1–13.

Amiri, A., Naraghi, M., Ahmadi, G., Soleymaniha, M., Shanbedi, M., 2018. FlatChem 8, 40–71.

Apte, A., Krishnamoorthy, A., Hachtel, J.A., Susarla, S., Idrobo, J.C., Nakano, A., Kalia, R.K., Vashishta, P., Tiwary, C.S., Ajayan, P.M., 2018. Chem. Mater. 30, 7262–7268.

Arnold, M.S., Green, A.A., Hulvat, J.F., Stupp, S.I., Hersam, M.C., 2006. Nat. Nanotechnol. 1, 60–65.

Arnold, M.S., Stupp, S.I., Hersam, M.C., 2005. Nano Lett. 5, 713–718.

Arter, J.A., Diaz, J.E., Donavan, K.C., Yuan, T., Penner, R.M., Weiss, G.A., 2012. Anal. Chem. 84, 2776–2783.

Arter, J.A., Taggart, D.K., McIntire, T.M., Penner, R.M., Weiss, G.A., 2010. Nano Lett. 10, 4858–4862.

Baboukani, A.R., Khakpour, I., Drozd, V., Allagui, A., Wang, C., 2019. J. Mater. Chem. A 7, 25548–25556.

Bach-Toledo, L., Hryniewicz, B.M., Marchesi, L.F., Dall'Antonia, L.H., Vidotti, M., Wolfart, F., 2020. Mater. Sci. Energy Technol. 3, 78–90.

Bai, R.G., Muthoosamy, K., Manickam, S., Hilal-Alnaqbi, A., 2019. Int. J. Nanomedicine 14, 5753.

Balasubramanian, K., Burghard, M., 2005. Small. 1.2, 180–192.

Bangar, M.A., Shirale, D.J., Purohit, H.J., Chen, W., Myung, N. V, Mulchandani, A., 2011. Electroanalysis 23, 371–379.

Bao, X., Ou, Q., Xu, Z., Zhang, Y., Bao, Q., Zhang, H., 2018. Adv. Mater. Technol. 3, 1800072.

Barsan, N., Weimar, U., 2003. J. Phys. Condens. Matter 15, R813.

Baryeh, K., Takalkar, S., Lund, M., Liu, G., 2017. Medical Biosensors for Point of Care (POC) Applications. Elsevier, pp. 3–25.

Bati, A.S.R., Yu, L., Batmunkh, M., Shapter, J.G., 2018. Nanoscale 10, 22087–22139.

Bennett, J.A., Agbere, I.B., Moesta, M., 2016. Electrochim. Acta 188, 111–119.

Bhasin, A., Ogata, A.F., Briggs, J.S., Tam, P.Y., Tan, M.X., Weiss, G.A., Penner, R.M., 2018. Nano Lett. 18, 3623–3629.

Bhasin, A., Sanders, E.C., Ziegler, J.M., Briggs, J.S., Drago, N.P., Attar, A.M., Santos, A.M., True, M.Y., Ogata, A.F., Yoon, D. V, Majumdar, S., Wheat, A.J., Patterson, S. V, Weiss, G.A., Penner, R.M., 2020. Anal. Chem. 92, 6654–6666.

Bhimanapati, G.R., Lin, Z., Meunier, V., Jung, Y., Cha, J., Das, S., Xiao, D., Son, Y., Strano, M.S., Cooper, V.R., Liang, L., Louie, S.G., Ringe, E., Zhou, W., Kim, S.S., Naik, R.R., Sumpter, B.G., Terrones, H., Xia, F., Wang, Y., Zhu, J., Akinwande, D., Alem, N., Schuller, J.A., Schaak, R.E., Terrones, M., Robinson, J.A., 2015. ACS Nano. 9.12, 11509–11539.

Bhushan, B., Luo, D., Schricker, S.R., Sigmund, W., Zauscher, S., 2014. Springer Science & Business Media.

Blair, E.O., Corrigan, D.K., 2019. Biosens. Bioelectron. 134, 57–67.

Bolotin, K.I., Sikes, K.J., Jiang, Z., Klima, M., Fudenberg, G., Hone, J., Kim, P., Stormer, H.L., 2008. Solid State Commun. 146, 351–355.

Bonaccorso, F., Colombo, L., Yu, G., Stoller, M., Tozzini, V., Ferrari, A.C., Ruoff, R.S., Pellegrini, V., 2015. Science. 347, 6217, 1246501.

Boukhvalov, D.W., Katsnelson, M.I., 2009. J. Phys. Condens. Matter 21, 344205.

Buchholz, D.B., Ma, Q., Alducin, D., Ponce, A., Jose-Yacaman, M., Khanal, R., Medvedeva, J.E., Chang, R.P.H., 2014. Chem. Mater. 26, 5401–5411.

Bunimovich, Y.L., Shin, Y.S., Yeo, W.-S., Amori, M., Kwong, G., Heath, J.R., 2006. J. Am. Chem. Soc. 128, 16323–16331.

Chandran, G.T., Li, X., Ogata, A., Penner, R.M., 2017. Anal. Chem. 89, 249–275.

Chang, H.-K., Ishikawa, F.N., Zhang, R., Datar, R., Cote, R.J., Thompson, M.E., Zhou, C., 2011. ACS Nano 5, 9883–9891.

Chang, J., Mao, S., Zhang, Y., Cui, S., Steeber, D.A., Chen, J., 2013. Biosens. Bioelectron. 42, 186–192.

Chang, J., Zhou, G., Gao, X., Mao, S., Cui, S., Ocola, L.E., Yuan, C., Chen, J., 2015. Sens. Bio-Sensing Res. 5, 97–104.

Chartuprayoon, N., Zhang, M., Bosze, W., Choa, Y.-H., Myung, N. V, 2015. Biosens. Bioelectron. 63, 432–443.

Chen, C.-P., Ganguly, A., Lu, C.-Y., Chen, T.-Y., Kuo, C.-C., Chen, R.-S., Tu, W.-H., Fischer, W.B., Chen, K.-H., Chen, L.-C., 2011. Anal. Chem. 83, 1938–1943.

Chen, E., Xu, W., Chen, J., Warner, J.H., 2020. Mater. Today Adv. 7, 100076.

Chen, H., Rim, Y.S., Wang, I.C., Li, C., Zhu, B., Sun, M., Goorsky, M.S., He, X., Yang, Y., 2017. ACS Nano 11, 4710–4718.

Chen, R.J., Zhang, Y., Wang, D., Dai, H., 2001. J. Am. Chem. Soc. 123.16, 3838–3839

Chen, X., Liu, Y., Fang, X., Li, Z., Pu, H., Chang, J., Chen, J., Mao, S., 2019. Biosens. Bioelectron. 126, 664–671.

Chen, Y., Ren, R., Pu, H., Chang, J., Mao, S., Chen, J., 2017a. Biosens. Bioelectron. 89, 505–510.

Chen, Y., Ren, R., Pu, H., Guo, X., Chang, J., Zhou, G., Mao, S., Kron, M., Chen, J., 2017b. Sci. Rep. 7, 1–8.

Cheng, S., Hotani, K., Hideshima, S., Kuroiwa, S., Nakanishi, T., Hashimoto, M., Mori, Y., Osaka, T., 2014. Materials. 7.4, 2490–2500.

Cheung, K.M., Abendroth, J.M., Nakatsuka, N., Zhu, B., Yang, Y., Andrews, A.M., Weiss, P.S., 2020. Nano Lett. 20, 5982–5990.

Chockla, A.M., Harris, J.T., Akhavan, V.A., Bogart, T.D., Holmberg, V.C., Steinhagen, C., Mullins, C.B., Stevenson, K.J., Korgel, B.A., 2011. J. Am. Chem. Soc. 133, 20914–20921.

Cohen-Karni, T., Casanova, D., Cahoon, J.F., Qing, Q., Bell, D.C., Lieber, C.M., 2012. Nano Lett. 12, 2639–2644.

Colombo, L., Venugopal, A., 2018.

Cui, Y., Duan, X., Hu, J., Lieber, C.M., 2000. J. Phys. Chem. B 104, 5213–5216.

Cui, Y., Wei, Q., Park, H., Lieber, C.M., 2001. Science. 293.5533, 1289–1292.

Curreli, M., Li, C., Sun, Y., Lei, B., Gundersen, M.A., Thompson, M.E., Zhou, C., 2005. J. Am. Chem. Soc. 127, 6922–6923.

Curreli, M., Zhang, R., Ishikawa, F.N., Chang, H., Cote, R.J., Zhou, C., Thompson, M.E., 2008. IEEE Trans. Nanotechnol. 7, 651–667.

Das, B.K., Tlili, C., Badhulika, S., Cella, L.N., Chen, W., Mulchandani, A., 2011. Chem. Commun. 47, 3793–3795.

Dasgupta, N.P., Sun, J., Liu, C., Brittman, S., Andrews, S.C., Lim, J., Gao, H., Yan, R., Yang, P., 2014. Adv. Mater. 26, 2137–2184.

Dattoli, E.N., Wan, Q., Guo, W., Chen, Y., Pan, X., Lu, W., 2007. Nano Lett. 7, 2463–2469.

Davis, K., Yarbrough, R., Froeschle, M., White, J., Rathnayake, H., 2019. RSC Adv. 9, 14638–14648.

De Volder, M.F.L., Tawfick, S.H., Baughman, R.H., Hart, A.J., 2013. Science. 339.611, 535-339.

Deng, S., Berry, V., 2016. Mater. Today 19, 197–212.

Ding, H., Ray, K.G., Ozolins, V., Asta, M., 2012. Phys. Rev. B 85, 12104.

Dorvel, B.R., Reddy, B., Go, J., Duarte Guevara, C., Salm, E., Alam, M.A., Bashir, R., 2012. ACS Nano 6, 6150–6164.

Duan, X., Li, Y., Rajan, N.K., Routenberg, D.A., Modis, Y., Reed, M.A., 2012. Nat. Nanotechnol. 7, 401–407.

Duan, X., Lieber, C.M., 2015. Nano Res. 8, 1–22.

Eatemadi, A., Daraee, H., Karimkhanloo, H., Kouhi, M., Zarghami, N., Akbarzadeh, A., Abasi, M., Hanifehpour, Y., Joo, S.W., 2014. Nanoscale Res. 9.1, 393.

Eckermann, A.L., Feld, D.J., Shaw, J.A., Meade, T.J., 2010. Coord. Chem. Rev. 254, 1769–1802.

Eda, G., Mattevi, C., Yamaguchi, H., Kim, H., Chhowalla, M., 2009. J. Phys. Chem. C 113, 15768–15771.

Elnathan, R., Kwiat, M., Pevzner, A., Engel, Y., Burstein, L., Khatchtourints, A., Lichtenstein, A., Kantaev, R., Patolsky, F., 2012. Nano Lett. 12.10, 5245–5254.

Fennell, J.F., Hamaguchi, H., Yoon, B., Swager, T.M., 2017. Sensors (Switzerland). 17.5, 982.

Gao, H., Sun, M., Lin, C., Wang, S., 2012. Electroanalysis 24, 2283–2290.

Gao, Z., Ducos, P., Ye, H., Zauberman, J., Sriram, A., Yang, X., Wang, Z., Mitchell, M.W., Lekkas, D., Brisson, D., Johnson, A.T.C., 2020. 2D Mater. 7.2, 024001.

Gao, Z., Jin, Z., Ji, Q., Tang, Y., Kong, J., Zhang, L., Li, Y., 2018. Carbon.128, 117–124.

García-Aljaro, C., Bangar, M.A., Baldrich, E., Muñoz, F.J., Mulchandani, A., 2010a. Biosens. Bioelectron. 25, 2309–2312.

García-Aljaro, C., Cella, L.N., Shirale, D.J., Park, M., Muñoz, F.J., Yates, M. V., Mulchandani, A., 2010b.. Biosens. Bioelectron. 26.4, 1437–1411.

Garnett, E.C., Yang, P., 2008. J. Am. Chem. Soc. 130, 9224–9225.

Georgakilas, V., Otyepka, M., Bourlinos, A.B., Chandra, V., Kim, N., Kemp, K.C., Hobza, P., Zboril, R., Kim, K.S., 2012. Chem. Rev. 112, 6156–6214.

Gilbonio, H.E., Hwang, M.T., Bashir, R., 2020. Macalester J. Phys. Astron. 8, 8.

Gong, H., Chen, F., Huang, Z., Gu, Y., Zhang, Q., Chen, Y., Zhang, Y., Zhuang, J., Cho, Y.-K., Fang, R.H., Gao, W., Xu, S., Zhang, L., 2019. ACS Nano 13, 3714–3722.

Green, A.A., Duch, M.C., Hersam, M.C., 2009. Nano Res. 2, 69–77.

Green, A.A., Hersam, M.C., 2009. Nat. Nanotechnol. 4, 64–70.

Guo, D.J., Abdulagatov, A.I., Rourke, D.M., Bertness, K.A., George, S.M., Lee, Y.C., Tan, W., 2010. Langmuir 26, 18382–18391.

Guo, T., Nikolaev, P., Thess, A., Colbert, D.T., Smalley, R.E., 1995. Chem. Phys. Lett. 243.1–2, 49–54.

Han, X., Feng, S., Zhao, Y., Li, L., Zhan, Z., Tao, Z., Fan, Y., Lu, W., Zuo, W., Fu, D., 2019. RSC Adv. 9, 1394–1402.

Hangarter, C.M., Bangar, M., Mulchandani, A., Myung, N. V, 2010. J. Mater. Chem. 20, 3131–3140.

Hatada, M., Tran, T.-T., Tsugawa, W., Sode, K., Mulchandani, A., 2019. Biosens. Bioelectron. 129, 254–259.

Heller, I., Chatoor, S., Männik, J., Zevenbergen, M.A.G., Dekker, C., Lemay, S.G., 2010. J. Am. Chem. Soc. 132.48, 17149-17156.

Heller, I., Janssens, A.M., Männik, J., Minot, E.D., Lemay, S.G., Dekker, C., 2008. Nano Lett. 8.2, 591–595.

Hussain, C.M., Keçili, R., 2020. Mod. Environ. Anal. Tech. Pollut. 199–222.

Hwang, M.T., Heiranian, M., Kim, Y., You, S., Leem, J., Taqieddin, A., Faramarzi, V., Jing, Y., Park, I., Van Der Zande, A.M., 2020. Nat. Commun. 11, 1–11.

Iijima, S., 1991. Nature. 354.6348, 56-58.

Islam, A., Lee, J., Feng, P.X.-L., 2018. J. Appl. Phys. 123, 25701.

Israelachvili, J.N., 2011. https://doi.org/10.1016/C2011-0-05119-0

Jariwala, D., Sangwan, V.K., Lauhon, L.J., Marks, T.J., Hersam, M.C., 2013. Chem. Soc. Rev. 42.7, 2824-2860.

Jiang, Z., Qing, Q., Xie, P., Gao, R., Lieber, C.M., 2012. Nano Lett. 12, 1711–1716.

Kaisti, M., 2017. Biosens. Bioelectron. 98, 437–448.

Kalantar-zadeh, K., Vijayaraghavan, A., Ham, M.-H., Zheng, H., Breedon, M., Strano, M.S., 2010. Chem. Mater. 22, 5660–5666.

Karajanagi, S.S., Vertegel, A.A., Kane, R.S., Dordick, J.S., 2004. Langmuir. 20.26, 11594–11599.

Khairir, N.S., Hussin, M.R.M., Nasir, I.M., Uz-Zaman, A.S.M.M., Abdullah, W.F.H., Zoolfakar, A.S., 2015. IOP Conference Series: Materials Science and Engineering. IOP Publishing, p. 12031.

Khan, K., Tareen, A.K., Aslam, M., Wang, R., Zhang, Y., Mahmood, A., Ouyang, Z., Zhang, H., Guo, Z., 2020. J. Mater. Chem. C 8, 387–440.

Kholghi Eshkalak, S., Chinnappan, A., Jayathilaka, W.A.D.M., Khatibzadeh, M., Kowsari, E., Ramakrishna, S., 2017. Appl. Mater. Today. 9, 372–386.

Kim, J., Campbell, A.S., de Ávila, B.E.-F., Wang, J., 2019. Nat. Biotechnol. 37, 389–406.

Kim, J., Sando, S., Cui, T., 2017. Proceedings of the ASME 2017 International Mechanical Engineering Congress and Exposition. Volume 2: Advanced Manufacturing. Tampa, Florida, USA. November 3–9, 2017. V002T02A072. ASME.

Kim, J.P., Lee, B.Y., Hong, S., Sim, S.J., 2008. Anal. Biochem. 381, 193–198.

Kim, K.H., Park, S.J., Park, C.S., Seo, S.E., Lee, J., Kim, J., Lee, S.H., Lee, S., Kim, J.-S., Ryu, C.-M., 2020. Biosens. Bioelectron. 167, 112514.

Kirste, R., Rohrbaugh, N., Bryan, I., Bryan, Z., Collazo, R., Ivanisevic, A., 2015. Electronic Biosensors Based on III-Nitride Semiconductors. Annu. Rev. Anal. Chem. 8, 149–169. https://doi.org/10.1146/annurev-anchem-071114-040247

Kong, J., Franklin, N.R., Zhou, C., Chapline, M.G., Peng, S., Cho, K., Dai, H., 2000. Science. 287.5453, 622–625.

Kou, L., Chen, C., Smith, S.C., 2015. J. Phys. Chem. Lett. 6, 2794–2805.

Krishnan, S.K., Singh, E., Singh, P., Meyyappan, M., Nalwa, H.S., 2019. RSC Adv. 9, 8778–8881.

Kulkarni, G.S., Zhong, Z., 2012. Nano Lett. 12, 719–723.

Kumar, P. V, Bardhan, N.M., Chen, G.-Y., Li, Z., Belcher, A.M., Grossman, J.C., 2016. Carbon. 100, 90–98.

Kutana, A., Penev, E.S., Yakobson, B.I., 2014. Nanoscale 6, 5820–5825.

Kwon, O.S., Kim, H., Ko, H., Lee, J., Lee, B., Jung, C.H., Choi, J.H., Shin, K., 2013. Carbon. 58. 116–127.

Lan, Y., Wang, Y., Ren, Z.F., 2011. Adv. Phys. 60.4, 553–678.

Laocharoensuk, R., Palaniappan, K., Smith, N.A., Dickerson, R.M., Werder, D.J., Baldwin, J.K., Hollingsworth, J.A., 2013. Nat. Nanotechnol. 8, 660–666.

Le, L.T., Ervin, M.H., Qiu, H., Fuchs, B.E., Lee, W.Y., 2011. Electrochem. commun. 13, 355–358.

Lee, H., Choi, J. Il, Park, J., Jang, S.S., Lee, S.W., 2020. Carbon. 167, 816–825.

Lee, I., Luo, X., Huang, J., Cui, X.T., Yun, M., 2012. Biosens. 2.2, 205–220.

Lee, J.-H., Park, S.-J., Choi, J.-W., 2019. Nanomaterials 9, 297.

Lee, J., Dak, P., Lee, Y., Park, H., Choi, W., Alam, M.A., Kim, S., 2014. Sci. Rep. 4, 7352.

Lee, J., Wang, C., Zhou, S., Chen, J., 2019. Procedia Manuf. 34, 19–25.

Lee, M.-G., Kim, J.-Y., 2012. Trans. Electr. Electron. Mater. 13, 165–170.

Lee, S.H., Kim, K.H., Seo, S.E., il Kim, M., Park, S.J., Kwon, O.S., 2020. J. Ind. Eng. Chem. 83, 29–34.

Lei, K.F., Yang, S.-I., Tsai, S.-W., Hsu, H.-T., 2015. Talanta 134, 264–270.

Lerner, M.B., D'Souza, J., Pazina, T., Dailey, J., Goldsmith, B.R., Robinson, M.K., Johnson, A.T.C., 2012. ACS Nano. 6.6, 5143–5249.

Lerner, M.B., Dailey, J., Goldsmith, B.R., Brisson, D., Charlie Johnson, A.T., 2013. Biosens. Bioelectron. 45, 163–167.

Li, C., Zhang, D., Liu, X., Han, S., Tang, T., Han, J., Zhou, C., 2003. Appl. Phys. Lett. 82, 1613–1615.

Li, D.O., Chu, X.S., Wang, Q.H., 2019. Langmuir 35, 5693–5701.

Li, J., Chen, C., Liu, S., Lu, J., Goh, W.P., Fang, H., Qiu, Z., Tian, B., Chen, Z., Yao, C., 2018. Chem. Mater. 30, 2742–2749.

Li, J., Luo, H., Zhai, B., Lu, R., Guo, Z., Zhang, H., Liu, Y., 2016. Sci. Rep. 6, 30361.

Li, J., Wu, Q., Wu, J., 2015. Handb. Nanoparticles 1–28.

Li, J., Zhang, Y., To, S., You, L., Sun, Y., 2011. ACS Nano. 5.8, 6661-6668.

Li, L., Yu, Y., Ye, G.J., Ge, Q., Ou, X., Wu, H., Feng, D., Chen, X.H., Zhang, Y., 2014. Nat. Nanotechnol. 9, 372–377.

Li, X., Liu, X., 2017. Nanoscale 9, 7320–7341.

Li, Z., Ezhilarasu, G., Chatzakis, I., Dhall, R., Chen, C.-C., Cronin, S.B., 2015. Nano Lett. 15, 3977–3982.

Li, Z., Rajendran, B., Kamins, T.I., Li, X., Chen, Y., Williams, R.S., 2005. Appl. Phys. A 80, 1257–1263.

Liang, Y., Huang, J., Zang, P., Kim, J., Hu, W., 2014. Appl. Surf. Sci. 322, 202–208.

Liao, Z., Zhang, Y., Li, Y., Miao, Y., Gao, S., Lin, F., Deng, Y., Geng, L., 2019. Biosens. Bioelectron. 126, 697–706.

Lin, Z., Carvalho, B.R., Kahn, E., Lv, R., Rao, R., Terrones, H., Pimenta, M.A., Terrones, M., 2016. 2D Mater. 3, 22002.

Liu, H., Duan, C., Yang, C., Chen, X., Shen, W., Zhu, Z., 2015. Mater. Sci. Eng. C 53, 43–49.

Liu, Q., Aroonyadet, N., Song, Y., Wang, X., Cao, X., Liu, Y., Cong, S., Wu, F., Thompson, M.E., Zhou, C., 2016. ACS Nano 10, 10117–10125.

Liu, Q., Liu, Y., Wu, F., Cao, X., Li, Z., Alharbi, M., Abbas, A.N., Amer, M.R., Zhou, C., 2018. ACS Nano 12, 1170–1178.

Liu, X., Ryder, C.R., Wells, S.A., Hersam, M.C., 2017. Small Methods 1.6, 1700143.

Long, Y.-Z., Li, M.-M., Gu, C., Wan, M., Duvail, J.-L., Liu, Z., Fan, Z., 2011. Prog. Polym. Sci. 36, 1415–1442.

Luo, J., Jang, H.D., Sun, T., Xiao, L., He, Z., Katsoulidis, A.P., Kanatzidis, M.G., Gibson, J.M., Huang, J., 2011. ACS Nano 5, 8943–8949.

Lv, R., Robinson, J.A., Schaak, R.E., Sun, D., Sun, Y., Mallouk, T.E., Terrones, M., 2015. Acc. Chem. Res. 48, 56–64.

Ma, X., Zachariah, M.R., Zangmeister, C.D., 2012. Nano Lett. 12, 486–489.

Maedler, C., Kim, D., Spanjaard, R.A., Hong, M., Erramilli, S., Mohanty, P., 2016. ACS Sensors 1, 696–701.

Mago, G., Kalyon, D.M., Fisher, F.T., 2009. J. Appl. Polym. Sci. 114.2, 1312–1319.

Mannhart, J., Schlom, D.G., 2010. Science. 327.5973, 1607–1611.

Mao, S., Chang, J., Pu, H., Lu, G., He, Q., Zhang, H., Chen, J., 2017. Chem. Soc. Rev. 46, 6872–6904.

Mao, S., Lu, G., Yu, K., Chen, J., 2010. Carbon. 48, 479–486.

Marcano, D.C., Kosynkin, D. V, Berlin, J.M., Sinitskii, A., Sun, Z., Slesarev, A., Alemany, L.B., Lu, W., Tour, J.M., 2010. ACS Nano 4, 4806–4814.

Masurkar, N., Varma, S., Mohana Reddy Arava, L., 2020. Electrochem 1, 260–277.

Mcbride, P.T., Janata, J., Comte, P.A., Moss, S.D., Johnson, C.C., 1978. Anal. Chim. Acta 101, 239–245.

Medina-Sánchez, M., Martínez-Domingo, C., Ramon, E., Merkoçi, A., 2014. Adv. Funct. Mater. 24, 6291–6302.

Meng, Z., Stolz, R.M., Mendecki, L., Mirica, K.A., 2019. Chem. Rev. 119, 478–598.

Mohammad, N.S., 2014. J. Phys. Condens. Matter 26, 423202.

Mohan, K., Donavan, K.C., Arter, J.A., Penner, R.M., Weiss, G.A., 2013. J. Am. Chem. Soc. 135, 7761–7767.

Moore, V.C., Strano, M.S., Haroz, E.H., Hauge, R.H., Smalley, R.E., Schmidt, J., Talmon, Y., 2003. Nano Lett. 3.10, 1379–1382.

Mu, X., Wang, J., Sun, M., 2019. Mater. Today Phys. 8, 92–111.

Mun, K.-S., Alvarez, S.D., Choi, W.-Y., Sailor, M.J., 2010. ACS Nano 4, 2070–2076.

Münzer, A.M., Seo, W., Morgan, G.J., Michael, Z.P., Zhao, Y., Melzer, K., Scarpa, G., Star, A., 2014. J. Phys. Chem. C 118, 17193–17199.

Nair, P.R., Alam, M.A., 2008. Nano Lett. 8, 1281–1285.

Nakatsuka, N., Yang, K.A., Abendroth, J.M., Cheung, K.M., Xu, X., Yang, H., Zhao, C., Zhu, B., Rim, Y.S., Yang, Y., Weiss, P.S., Stojanović, M.N., Andrews, A.M., 2018. Science. 362, 319–324.

Nessim, G.D., 2010. Nanoscale. 2.8, 1306–1323.

Novoselov, K.S., Geim, A.K., Morozov, S. V, Jiang, D., Zhang, Y., Dubonos, S. V, Grigorieva, I. V, Firsov, A.A., 2004. Science. 306.5969, 666–669.

O'Connell, M.J., Boul, P., Ericson, L.M., Huffman, C., Wang, Y., Haroz, E., Kuper, C., Tour, J., Ausman, K.D., Smalley, R.E., 2001. Chem. Phys. Lett. 342.3–4, 265-271.

Ogata, A.F., Edgar, J.M., Majumdar, S., Briggs, J.S., Patterson, S. V, Tan, M.X., Kudlacek, S.T., Schneider, C.A., Weiss, G.A., Penner, R.M., 2017. Anal. Chem. 89, 1373–1381.

Pan, Z.W., Dai, S., Rouleau, C.M., Lowndes, D.H., 2005. Angew. Chemie Int. Ed. 44, 274–278.

Park, C.S., Lee, C., Kwon, O.S., 2016. Polym. 8.7, 249.

Park, H., Han, G., Lee, S.W., Lee, H., Jeong, S.H., Naqi, M., AlMutairi, A., Kim, Y.J., Lee, J., Kim, W., 2017. ACS Appl. Mater. Interfaces 9, 43490–43497.

Pei, S., Cheng, H.-M., 2012. Carbon. 50.9, 3210–3228.

Peigney, A., Laurent, C., Flahaut, E., Bacsa, R.R., Rousset, A., 2001. Carbon. 39.4, 507–514.

Peixoto, A.C., Silva, A.F., 2017. Bioinspired Materials for Medical Applications. Elsevier, pp. 297–329.

Penner, R.M., 2012. Annu. Rev. Anal. Chem. 5, 461–485.

Pham, T., Li, G., Bekyarova, E., Itkis, M.E., Mulchandani, A., 2019. ACS Nano 13, 3196–3205.

Ramanathan, K., Bangar, M.A., Yun, M., Chen, W., Mulchandani, A., Myung, N. V, 2004. Nano Lett. 4, 1237–1239.

Ramanathan, K., Bangar, M.A., Yun, M., Chen, W., Myung, N. V, Mulchandani, A., 2005. J. Am. Chem. Soc. 127, 496–497.

Ramanujam, J., Shiri, D., Verma, A., 2011. Mater. Express 1, 105–126.

Ramnani, P., Gao, Y., Ozsoz, M., Mulchandani, A., 2013. Anal. Chem. 85, 8061–8064.

Ramnani, P., Saucedo, N.M., Mulchandani, A., 2016. Chemosphere 143, 85–98.

Rashid, M.H.O., Ralph, S.F., 2017. Nanomaterials. 7.5, 99.

Regonda, S., Tian, R., Gao, J., Greene, S., Ding, J., Hu, W., 2013. Biosens. Bioelectron. 45, 245–251.

Rim, Y.S., 2020. J. Inf. Disp. 1–8.

Rim, Y.S., Bae, S.H., Chen, H., Yang, J.L., Kim, J., Andrews, A.M., Weiss, P.S., Yang, Y., Tseng, H.R., 2015. ACS Nano 9, 12174–12181.

Sahoo, P., Suresh, S., Dhara, S., Saini, G., Rangarajan, S., Tyagi, A.K., 2013. Biosens. Bioelectron. 44, 164–170.

Sang, S., Wang, Y., Feng, Q., Wei, Y., Ji, J., Zhang, W., 2016. Crit. Rev. Biotechnol. 36, 465–481.

Sarkar, D., 2019. Fundamentals and Sensing Applications of 2D Materials. Elsevier, pp. 329–377.

Sarkar, D., Liu, W., Xie, X., Anselmo, A.C., Mitragotri, S., Banerjee, K., 2014. ACS Nano. 8.4, 3992–4003.

Saucedo, N.M., Gao, Y., Pham, T., Mulchandani, A., 2018. Biosensors. 8.3, 63.

Şerban, I., Enesca, A., 2020. Front. Chem. 8, 1–8.

Shanmugam, N.R., Muthukumar, S., Prasad, S., 2017. Futur. Sci. OA 3, FSO196.

Shao, W., Burkert, S.C., White, D.L., Scott, V.L., Ding, J., Li, Z., Ouyang, J., Lapointe, F., Malenfant, P.R.L., Islam, K., Star, A., 2019. Nanoscale. 11.28, 13397–13406.

Shen, Y., Tran, T.-T., Modha, S., Tsutsui, H., Mulchandani, A., 2019. Biosens. Bioelectron. 130, 367–373.

Shi, Y., Li, H., Li, L.-J., 2015. Chem. Soc. Rev. 44, 2744–2756.

Shirale, D.J., Bangar, M.A., Park, M., Yates, M. V, Chen, W., Myung, N. V, Mulchandani, A., 2010. Environ. Sci. Technol. 44, 9030–9035.

Shoorideh, K., Chui, C.O., 2014. Proc. Natl. Acad. Sci. 111, 5111–5116.

Shu, G.J., Chou, F.C., 2012. arXiv Prepr. arXiv1212.5982.

Silva, G.O., Michael, Z.P., Bian, L., Shurin, G. V., Mulato, M., Shurin, M.R., Star, A., 2017. ACS Sensors. 2.8, 1128–1132.

Simmons, T.J., Bult, J., Hashim, D.P., Linhardt, R.J., Ajayan, P.M., 2009. ACS Nano. 3.4, 865-870.

Song, E., Tortorich, R.P., da Costa, T.H., Choi, J.-W., 2015. Microelectron. Eng. 145, 143–148.

Sresht, V., Pádua, A.A.H., Blankschtein, D., 2015. ACS Nano 9, 8255–8268.

Stankovich, S., Dikin, D.A., Piner, R.D., Kohlhaas, K.A., Kleinhammes, A., Jia, Y., Wu, Y., Nguyen, S.T., Ruoff, R.S., 2007. Carbon. 45.7, 1558–1565.

Star, A., Stoddart, J.F., Steuerman, D., Diehl, M., Boukai, A., Wong, E.W., Yang, X., Chung, S.W., Choi, H., Heath, J.R., 2001. Angew. Chemie - Int. Ed. 113.9, 1771–1775.

Subramanian, S., Aschenbach, K.H., Evangelista, J.P., Najjar, M.B., Song, W., Gomez, R.D., 2012. Biosens. Bioelectron. 32, 69–75.

Sun, J., Liu, C., Yang, P., 2011. J. Am. Chem. Soc. 133, 19306–19309.

Sun, Z., Liao, T., Dou, Y., Hwang, S.M., Park, M.-S., Jiang, L., Kim, J.H., Dou, S.X., 2014. Nat. Commun. 5, 1–9.

Taleat, Z., Khoshroo, A., Mazloum-Ardakani, M., 2014. Microchim. Acta. 181.9–10, 865–891.

Tan, F., Saucedo, N.M., Ramnani, P., Mulchandani, A., 2015. Environ. Sci. Technol. 49, 9256–9263.

Tang, Q., Jiang, D., 2015. Chem. Mater. 27, 3743–3748.

Thakur, B., Zhou, G., Chang, J., Pu, H., Jin, B., Sui, X., Yuan, X., Yang, C.-H., Magruder, M., Chen, J.,

2018. Biosens. Bioelectron. 110, 16–22.

Tian, B., Cohen-Karni, T., Qing, Q., Duan, X., Xie, P., Lieber, C.M., 2010. Science. 329.5993, 830–834.

Tian, R., Regonda, S., Gao, J., Liu, Y., Hu, W., 2011. Lab Chip 11, 1952–1961.

Tlili, C., Myung, N. V, Shetty, V., Mulchandani, A., 2011. Biosens. Bioelectron. 26, 4382–4386.

Torrisi, F., Coleman, J.N., 2014. Nat. Nanotechnol. 9, 738–739.

Tran, D.P., Pham, T.T.T., Wolfrum, B., Offenhäusser, A., Thierry, B., 2018. Materials. 11.5, 785.

Tran, T.-T., Clark, K., Ma, W., Mulchandani, A., 2020. Biosens. Bioelectron. 147, 111766.

Tsang, D.K.H., Lieberthal, T.J., Watts, C., Dunlop, I.E., Ramadan, S., Armando, E., Klein, N., 2019. Sci. Rep. 9, 1–10.

Tu, J., Gan, Y., Liang, T., Hu, Q., Wang, Q., Ren, T., Sun, Q., Wan, H., Wang, P., 2018. Front. Chem. 6, 333.

Van Tuan, C., Tuan, M.A., Van Hieu, N., Trung, T., 2012. Curr. Appl. Phys. 12, 1011–1016.

Vedala, H., Chen, Y., Cecioni, S., Imberty, A., Vidal, S., Star, A., 2011. Nano Lett. 11.1, 170–175.

Viswanathan, S., Narayanan, T.N., Aran, K., Fink, K.D., Paredes, J., Ajayan, P.M., Filipek, S., Miszta, P., Tekin, H.C., Inci, F., 2015. Mater. Today 18, 513–522.

Vu, C.-A., Chen, W.-Y., 2019. Sensors 19, 4214.

Wang, C., Zhang, J., Ryu, K., Badmaev, A., De Arco, L.G., Zhou, C., 2009. Nano Lett. 9.12, 4285–4291.

Wang, D., Qian, F., Yang, C., Zhong, Z., Lieber, C.M., 2004. Nano Lett. 4, 871–874.

Wang, G., Wang, Z., Liu, Z., Xue, J., Xin, G., Yu, Q., Lian, J., Chen, M.Y., 2015.. Chem. Eng. J. 260, 582–589.

Wang, J., Chan, S., Carlson, R.R., Luo, Y., Ge, G., Ries, R.S., Heath, J.R., Tseng, H.-R., 2004. Nano Lett. 4, 1693–1697.

Wang, J., Xu, G., Zhang, Xu, Lv, J., Zhang, Xinyi, Zheng, Z., Wu, Y., 2015. Dalt. Trans. 44, 7662–7672.

Wang, X., Zhu, Y., Olsen, T.R., Sun, N., Zhang, W., Pei, R., Lin, Q., 2018. Electrochim. Acta 290, 356–363.

Wang, Y., Li, Z., Wang, J., Li, J., Lin, Y., 2011. Trends Biotechnol. 29, 205–212.

Wang, Z., Hao, Z., Yu, S., De Moraes, C.G., Suh, L.H., Zhao, X., Lin, Q., 2019. Adv. Funct. Mater. 29, 1905202.

Wasik, D., Mulchandani, A., Yates, M. V, 2018. Sensors 18, 2641.

Wasik, D., Mulchandani, A., Yates, M. V, 2017. Biosens. Bioelectron. 91, 811–816.

Weizmann, Y., Chenoweth, D.M., Swager, T.M., 2011. J. Am. Chem. Soc. 133.10, 3238–3241.

Williams, E.H., Davydov, A. V, Oleshko, V.P., Steffens, K.L., Levin, I., Lin, N.J., Bertness, K.A., Manocchi, A.K., Schreifels, J.A., Rao, M. V, 2014. Surf. Sci. 627, 23–28.

Wilson, J.A., Yoffe, A.D., 1969. Adv. Phys. 18, 193–335.

Woomer, A.H., Farnsworth, T.W., Hu, J., Wells, R.A., Donley, C.L., Warren, S.C., 2015. ACS Nano 9, 8869–8884.

Wordofa, D.N., Ramnani, P., Tran, T.T., Mulchandani, A., 2016. Analyst. 141.9, 2756–2760.

Wu, G., Dai, Z., Tang, X., Lin, Z., Lo, P.K., Meyyappan, M., Lai, K.W.C., 2017. Adv. Healthc. Mater. 6, 1700736.

Wu, J., Lu, Y., Wu, Z., Li, S., Zhang, Q., Chen, Z., Jiang, J., Lin, S., Zhu, L., Li, C., 2018. Sensors Actuators B Chem. 261, 279–287.

Wu, W., De, D., Chang, S.-C., Wang, Y., Peng, H., Bao, J., Pei, S.-S., 2013. Appl. Phys. Lett. 102, 142106.

Xia, F., Wang, H., Jia, Y., 2014. Nat. Commun. 5, 1–6.

Xiao, X., Song, H., Lin, S., Zhou, Y., Zhan, X., Hu, Z., Zhang, Q., Sun, J., Yang, B., Li, T., 2016. Nat. Commun. 7, 1–8.

Xu, L., Shoaei, N., Jahanpeyma, F., Zhao, J., Azimzadeh, M., Al, K.T., 2020. Biosens. Bioelectron. 112222.

Xu, S., Wang, Z.L., 2011. Nano Res. 4, 1013–1098.

Xu, Y., Pehrsson, P.E., Chen, L., Zhang, R., Zhao, W., 2007. Double-stranded DNA single-walled carbon nanotube hybrids for optical hydrogen peroxide and glucose sensing. J. Phys. Chem. C. 111.24, 8638–8643.

Yan, J.-A., Yang, L., Chou, M.Y., 2007. Phys. Rev. B 76, 115319.

Yang, N., Chen, X., Ren, T., Zhang, P., Yang, D., 2015. Sensors Actuators B Chem. 207, 690–715.

Yao, M.-S., Li, W.-H., Xu, G., 2021. Coord. Chem. Rev. 426, 213479.

Yeo, W.-S., Yousaf, M.N., Mrksich, M., 2003. J. Am. Chem. Soc. 125, 14994–14995.

Zafar, S., D'Emic, C., Jagtiani, A., Kratschmer, E., Miao, X., Zhu, Y., Mo, R., Sosa, N., Hamann, H., Shahidi, G., 2018. ACS Nano 12, 6577–6587.

Zaid, M.H.M., Abdullah, J., Yusof, N.A., Sulaiman, Y., Wasoh, H., Noh, M.F.M., Issa, R., 2017. Sensors Actuators B Chem. 241, 1024–1034.

Zang, J., Ryu, S., Pugno, N., Wang, Q., Tu, Q., Buehler, M.J., Zhao, X., 2013. Nat. Mater. 12, 321–325.

Zhang, A., Lieber, C.M., 2016. Chem. Rev. 116, 215–257.

Zhang, G.-J., Ning, Y., 2012. Anal. Chim. Acta 749, 1–15.

Zhang, G.-J., Zhang, L., Huang, M.J., Luo, Z.H.H., Tay, G.K.I., Lim, E.-J.A., Kang, T.G., Chen, Y., 2010. Sensors Actuators B Chem. 146, 138–144.

Zhang, H., 2015. ACS Nano 9, 9451–9469.

Zhang, J.X.J., Hoshino, K., 2014. Mol. Sensors Nanodevices Princ. Des. Appl. Biomed. Eng. 321–414.

Zhang, W., Pan, Z., Yang, F.K., Zhao, B., 2015. Adv. Funct. Mater. 25, 1588–1597.

Zhang, X., Lu, W., Zhou, G., Li, Q., 2020. Adv. Mater. 32.5, 1902028.

Zhang, Y.I., Zhang, L., Zhou, C., 2013. Acc. Chem. Res. 46, 2329–2339.

Zhang, Y.J., Yoshida, M., Suzuki, R., Iwasa, Y., 2015. 2D Mater. 2, 44004.

Zhao, S., Nguyen, H.P.T., Kibria, M.G., Mi, Z., 2015. Prog. Quantum Electron. 44, 14–68.

Zheng, G., Gao, X.P.A., Lieber, C.M., 2010. Nano Lett. 10, 3179–3183.

Zheng, G., Lieber, C.M., 2011. Nanoproteomics. Springer, pp. 223–237.

Zheng, M., Jagota, A., Semke, E.D., Diner, B.A., McLean, R.S., Lustig, S.R., Richardson, R.E., Tassi,

N.G., 2003. Nat. Mater. 2.5, 338–342.

Zhou, J., Lin, J., Huang, X., Zhou, Y., Chen, Y., Xia, J., Wang, H., Xie, Y., Yu, H., Lei, J., 2018. Nature 556, 355–359.

Zhou, L., He, B., Yang, Y., He, Y., 2014. Rsc Adv. 4, 32570–32578.

Zhou, Y., Fang, Y., Ramasamy, R.P., 2019. Sensors. 19.2, 392.

Zhu, C., Du, D., Lin, Y., 2015. 2D Mater. 2, 32004.

Zhu, Y., Murali, S., Cai, W., Li, X., Suk, J.W., Potts, J.R., Ruoff, R.S., 2010. Adv. Mater. 22, 3906–3924.

Zong, X., Yan, H., Wu, G., Ma, G., Wen, F., Wang, L., Li, C., 2008. J. Am. Chem. Soc. 130, 7176–7177.